

## High Resolution Search for KBO Binaries from *New Horizons*

H. A. WEAVER,<sup>1</sup> S. B. PORTER,<sup>2</sup> J. R. SPENCER,<sup>2</sup> AND THE *New Horizons* SCIENCE TEAM

<sup>1</sup>*Johns Hopkins University Applied Physics Laboratory, 11100 Johns Hopkins Road, Laurel, MD 20723-6099, USA*

<sup>2</sup>*Southwest Research Institute, 1050 Walnut Street, Suite 300, Boulder, CO 80302, USA*

(Received August 15, 2021; Revised January 2, 2022; Accepted January 15, 2022)

Submitted to Planetary Science Journal

### ABSTRACT

Using the *New Horizons* LORRI camera, we searched for satellites near five Kuiper belt objects (KBOs): four cold classicals (CCs: 2011 JY<sub>31</sub>, 2014 OS<sub>393</sub>, 2014 PN<sub>70</sub>, 2011 HZ<sub>102</sub>) and one scattered disk object (SD: 2011 HK<sub>103</sub>). These objects were observed at distances of 0.092-0.290 au from the *New Horizons* spacecraft, achieving spatial resolutions of 136-430 km (resolution is  $\sim 2$  camera pixels), much higher than possible from any other facilities. Here we report that CC 2011 JY<sub>31</sub> is a binary system with roughly equal brightness components, CC 2014 OS<sub>393</sub> is likely an equal brightness binary system, while the three other KBOs did not show any evidence of binarity. The JY<sub>31</sub> binary has a semi-major axis of  $198.6 \pm 2.9$  km, an orbital inclination of  $61^\circ 34' \pm 1^\circ 34'$ , and an orbital period of  $1.940 \pm 0.002$  d. The OS<sub>393</sub> binary objects have an apparent separation of  $\sim 150$  km, making JY<sub>31</sub> and OS<sub>393</sub> the tightest KBO binary systems ever resolved. Both HK<sub>103</sub> and HZ<sub>102</sub> were detected with  $\text{SNR} \approx 10$ , and our observations rule out equal brightness binaries with separations larger than  $\sim 430$  km and  $\sim 260$  km, respectively. The spatial resolution for PN<sub>70</sub> was  $\sim 200$  km, but this object had  $\text{SNR} \approx 2.5$ –3, which limited our ability to probe its binarity. The binary frequency for the CC binaries probed in our small survey (67%, not including PN<sub>70</sub>) is consistent with the high binary frequency suggested by larger surveys of CCs (Fraser et al. 2017a,b; Noll et al. 2020) and recent planetesimal formation models (Nesvorný et al. 2021), but we extend the results to smaller orbit semi-major axes and smaller objects than previously possible.

### 1. INTRODUCTION

The *New Horizons* (NH) spacecraft has been traversing the Kuiper belt since 2015. The close flyby of Pluto on 2015 July 14 at a distance of  $\sim 12,500$  km revolutionized our understanding of that dwarf planet and its satellites (cf., Stern et al. 2018). On 2019 January 1, the *New Horizons* spacecraft passed within 3600 km of the cold classical (CC) Kuiper belt object (KBO) (486958)

Arrokoth, conducting ultraviolet, visible, near-infrared, and radio investigations with unprecedented resolution and sensitivity that have revealed unique results on planetesimal formation and evolution in the distant solar system (Stern et al. 2019; Grundy et al. 2020; McKinnon et al. 2020; Spencer et al. 2020). More generally, *New Horizons* has enabled observations of dozens of KBOs at unique geometries, including at large solar phase angles not possible from the inner solar system (e.g., Porter et al. 2016; Verbiscer et al. 2019, 2022) and at distances from the spacecraft that provide higher spatial resolution than available from Earth, or Earth-orbiting, facilities. Here we describe how this latter capability has been exploited to provide sensitive searches for possible satellites of KBOs passing within 0.3 au of the *New Horizons* spacecraft when the spatial resolution exceeded that available from the *Hubble Space Telescope* (*HST*) by a factor  $\geq 6$ . The *New Horizons* flyby observations of Arrokoth revealed it to be a contact binary with two distinct lobes, but sensitive searches did not uncover any other satellites larger than a few hundred meters in diameter within a few hundred kilometers of the main body (Stern et al. 2019).

These *New Horizons* high resolution KBO satellite searches were conducted using the LOng Range Reconnaissance Imager (LORRI), which is a panchromatic (360–910 nm), narrow angle (field of view=FOV=0.291°), high spatial resolution (pixel scale=IFOV=1"02), Ritchey-Chrétien telescope with a CCD in its focal plane that is used for both science observations and optical navigation (Cheng et al. 2008; Weaver et al. 2020). For the highest resolution LORRI observations, like those discussed here, all optically active pixels are read out from the CCD (“1×1” format with 1024×1024 optically active pixels). When used in 1×1 format, and employing a typical exposure time of 150 ms to prevent pointing smear, LORRI can achieve a signal-to-noise ratio (SNR) of  $\sim 5$  for unresolved targets with  $V \leq 12.6$ . However, the pixels can also be re-binned by a factor of 4 in each direction (i.e., column and row directions) during CCD readout (“4×4” format with 256×256 optically active pixels), which reduces the data volume by a factor of 16 and results in an effective pixel size of IFOV=4"08. By employing 4×4 mode, a special spacecraft tracking mode, exposure times  $\geq 30$  s, and co-addition of  $\sim 100$  images, LORRI can detect unresolved targets down to  $V \approx 22$  with SNR  $\approx 5$ . This latter capability has been used extensively to measure KBO phase curves and light curves over wide ranges of solar phase angles (Porter et al. 2016; Verbiscer et al. 2019, 2022), which can only be achieved by a facility in the outer solar system.

The five KBOs discussed here were observed in both 1×1 and 4×4 format. The 1×1 observations were conducted primarily to search for potential satellites at high spatial resolution and are the main subject of this paper. Preliminary results from this program were discussed in Weaver et al. (2019), and the discovery that JY<sub>31</sub> is the tightest known KBO binary system was announced in Porter et al. (2020). The 4×4 observations were conducted to measure light curves, phase curves, and to refine the orbit solutions for these KBOs via astrometry; the details of the 4×4 observations are discussed in a separate paper (Porter et al. 2022).

For the LORRI 1×1 observations, hundreds of images had to be co-added, and longer than usual exposure times (500 ms) were needed to reach the sensitivity required to detect these small and faint KBOs, which had  $V \approx 14.5 - 17.3$ . We employed a special windowing technique to restrict the sizes of the images sent back to the Earth, which reduced the downlinked data volumes to  $\sim 20\%$  of their full-size values. The special techniques applied to these high resolution KBO observations are described further below.

**Table 1.** KBO Properties

Target	Class	a	e	i	$H_0$	$p_V$	$d_N$
		(au)		(deg)			(km)
2011 HK <sub>103</sub>	SD	53.07	0.311	6.43	8.4	0.08	99
2011 JY <sub>31</sub>	CC	43.95	0.059	2.61	8.8	0.15	60
2011 HZ <sub>102</sub>	CC	43.18	0.0061	2.39	9.2	0.15	50
2014 OS <sub>393</sub>	CC	43.94	0.032	3.81	10.1	0.15	33
2014 PN <sub>70</sub>	CC	44.04	0.050	4.12	10.3	0.15	30

NOTE—“Target” is the IAU KBO designation. “Class” refers to the KBO dynamical class: “CC” is short for “cold classical” and “SD” is short for “scattered disk”. “a”, “e”, “i” are the semi-major axis, eccentricity, and inclination angle, respectively, of the KBO’s orbit. “ $H_0$ ” is the KBO’s absolute  $V$ -mag from the Minor Planet Center. “ $p_V$ ” is the KBO’s assumed  $V$ -band geometric albedo based on its dynamical class. “ $d_N$ ” is the KBO’s estimated diameter. See the text for further details.

## 2. OBSERVATIONS

We observed five KBOs, which included four CCs and one scattered disk object (SD). All of these KBOs were discovered during dedicated searches for potential *New Horizons* observational targets: three (2011 HZ<sub>102</sub>, 2011 JY<sub>31</sub>, 2011 HK<sub>103</sub>) were discovered during a ground-based survey program and two (2014 OS<sub>393</sub>, 2014 PN<sub>70</sub>) were discovered during a search with *HST* (Spencer et al. 2015). Arrokoth, the target of a *New Horizons* mission close flyby campaign, was also discovered by that same *HST* program. OS<sub>393</sub> and PN<sub>70</sub> were potential close flyby *New Horizons* targets, but they required much more fuel to reach than Arrokoth and had later arrival times, so they were dropped from consideration.

Some key properties of these KBOs are provided in Table 1. The dynamical class assignments follow the standard conventions (Gladman et al. 2008; Noll et al. 2008b). The orbital parameters and absolute visual magnitudes ( $H_0$ ) are taken from the Minor Planet Center. The geometric albedos have not been measured for these KBOs, so we used representative values for their dynamical classes. For HK<sub>103</sub> we use the average geometric albedo derived from *Herschel* observatory observations of SD KBOs (Lacerda et al. 2014). For the CC KBOs, we use the average geometric albedo derived from *Herschel* observatory observations of CCs (Vilenius et al. 2014). We note that the reported geometric albedo of CC Arrokoth is  $0.21^{+0.05}_{-0.04}$  (Hofgartner et al. 2021), which is slightly larger than, but consistent within the error bars, the average CC value. The approximate effective diameters ( $d_N$ ) are derived from the listed  $H_0$  values and geometric albedos. Further details on these KBOs are discussed elsewhere (Verbiscer et al. 2019; Porter et al. 2022). All of the KBOs discussed here are small ( $\lesssim 100$  km in diameter) and require large telescopes ( $\gtrsim 6.5$  m) when observed from the vicinity of the Earth.

The LORRI  $1\times 1$  observations of these KBOs posed a number of technical challenges, principally involving sensitivity limitations and downlink data volume (DLDV) considerations. Pointing drift during observations limits the sensitivity achieved by individual images; exposures that are too long allow the target to move across multiple pixels thereby lowering the signal accumulated in the peak pixel and reducing the SNR. Pointing control on the *New Horizons* spacecraft is established by firing hydrazine thrusters and monitoring the response autonomously using star locations derived from a *New Horizons* attitude star tracker (AST)<sup>1</sup> and rates of motion derived from an inertial measurement unit (IMU)<sup>2</sup>. During these  $1\times 1$  KBO observations, the pointing was controlled to lie within a “deadband” of  $\pm 250 \mu\text{rad}$  ( $\pm 52''$ ) centered on the commanded target location in the LORRI field-of-view (FOV), always the center of the FOV (i.e., the LORRI “boresight”) for these cases. The total rate of motion (summed over all 3 directions, including spacecraft roll) was controlled to be  $\leq 38 \mu\text{rad s}^{-1}$  ( $\leq 7.8 \text{ s}^{-1}$ ). Whenever the pointing starts to breach these location or rate limits during an observation, the spacecraft’s attitude control system (ACS) fires the thrusters to maintain the pointing within these specified deadbands, typically at the rate of  $\sim 6$  thruster firings per minute. Thus, the pointing drifts during an observation within a box whose width is  $\pm 52''$  about the commanded location. This drift is taken into account when shifting and co-adding multiple images to produce more sensitive composites, as described later. The *New Horizons* pointing control system (see [Rogers et al. 2016](#)) has been stable with essentially identical performance over the entire mission duration.

One important consideration for our program was the choice of an exposure time that maximizes sensitivity while mitigating image smear caused by pointing drift. Typically, the pointing for observations using the control parameters discussed above drifts at an average rate of  $\sim 25 \mu\text{rad s}^{-1}$  ( $\sim 5 \text{ s}^{-1}$ ). Given that the intrinsic point spread function (PSF) of LORRI is  $\sim 2.5$  pixels (FWHM for the best-fit 2-dimensional gaussian; see [Weaver et al. \(2020\)](#)), we usually pick exposure times of  $\leq 150$  ms to keep the image smear  $\leq 1$  pixel. For these faint KBO targets, however, we increased the exposure time to 500 ms, which improves the single image sensitivity by a factor  $\sim 3$  while only modestly blurring the PSF. The pointing drifts for the KBO observations discussed here are consistent with what has been seen throughout the mission; an example is provided in [Figure 1](#).

The individual images taken with an exposure time of 500 ms achieve a sensitivity limit (SNR=5) on unresolved targets of  $V \approx 13.6$ , which is approximately 1 mag fainter than can be achieved using an exposure time of 150 ms. However, the KBOs targeted in this program were predicted to have  $V = 15.7\text{-}16.1$ , which requires co-adding at least 100 images to achieve detections of the fainter objects, much less provide a sensitive search for satellites. But downlinking hundreds of full LORRI  $1\times 1$  images would be prohibitively expensive; a single compressed LORRI image produces a DLDV of  $\sim 5$  Mbits and requires  $\sim 1$  h of 70 m antenna time from NASA’s Deep Space Network (DSN). Thus, each image was windowed to reduce the DLDV by a factor of  $\sim 5$ , while still retaining a large enough portion of the LORRI FOV to enable accurate astrometric solutions using stars captured in the windowed portion of image. Since the KBOs themselves couldn’t be detected in single images, producing an astrometric solution based on the detected stars is critical for enabling accurate co-addition of the images. (The pointing information from the spacecraft’s ACS isn’t accurate enough for this purpose.) In practice, we chose observation times when at least one star with  $V \leq 13$  was within

<sup>1</sup> There are two ASTs for redundancy, but only one is active at a time. Both ASTs employ CCD detectors.

<sup>2</sup> There are two IMUs for redundancy, but only one is active at a time. Each IMU is comprised of three laser ring gyros mounted orthogonally to each other.

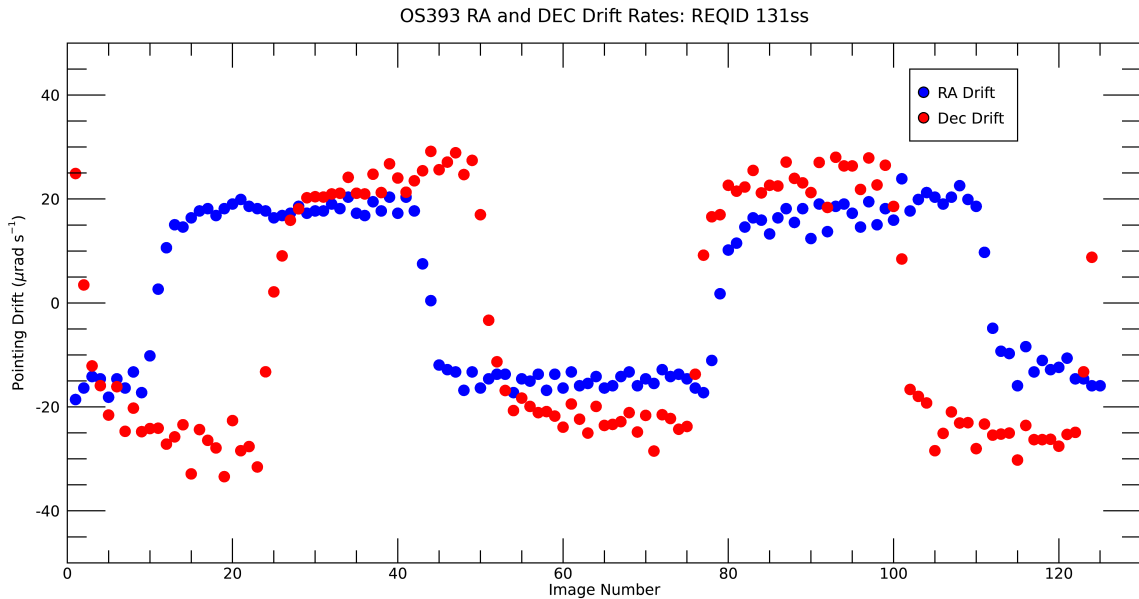


**Figure 1.** RA and DEC drift rates are displayed for the 125 images taken during the observations of OS<sub>393</sub> for REQID 131ss. The pointing drifts within a deadband of  $\pm 250 \mu\text{rad}$  ( $\pm 52''$ ) centered on the commanded target ephemeris location. Hydrazine thrusters fire to maintain the pointing within the deadband; the times of thruster firings are associated with abrupt changes in either the RA or DEC drift rates in this plot. The mean total plane-of-sky drift rate for this set of observations was  $27.34 \pm 4.51 \mu\text{rad s}^{-1}$  ( $5.64 \pm 0.93 \text{ arcsec s}^{-1}$ ), which is typical for *New Horizons* observations.

the same window containing the targeted KBO, something that was achieved for the vast majority of the images collected in this program. The only exception was PN<sub>70</sub>, which landed slightly outside the specified window for 229 of the 500 images taken owing to the large spatial separation between the KBO and the single bright nearby star. The window selection details for a more typical set of observations (in this case REQID 131ss for OS<sub>393</sub>; “REQID” is one of the FITS keywords for LORRI images used as a target identifier) are provided in Figure 2.

For each KBO discussed here, *New Horizons* took four sets of 125 LORRI  $1 \times 1$  images, with an exposure time of 500 ms for each image taken at 1 second cadence. Thus, it took 125 seconds to complete each set. Two sets of 125 images, separated by  $\sim 5$ -13 minutes, were taken the same day, then two more identical sets of 125 images each were taken 1 to 4 days later, depending on the target (see Table 2). For all observations, *New Horizons* was tracking the KBO using the target’s ephemeris, but the pointing drifted from image to image, as discussed above. Owing to onboard data management considerations, which were exacerbated by the Arrokoth flyby on New Year’s Day 2019, the full KBO images had to be deleted from the solid state recorder (SSR)<sup>3</sup> before the windowed portions could be downlinked. The downlink of the windowed images from the LORRI  $1 \times 1$  program was not completed until April 2020.

<sup>3</sup> There are two SSRs for redundancy, and the raw KBO images had to be stored on SSR2, which is not normally powered.

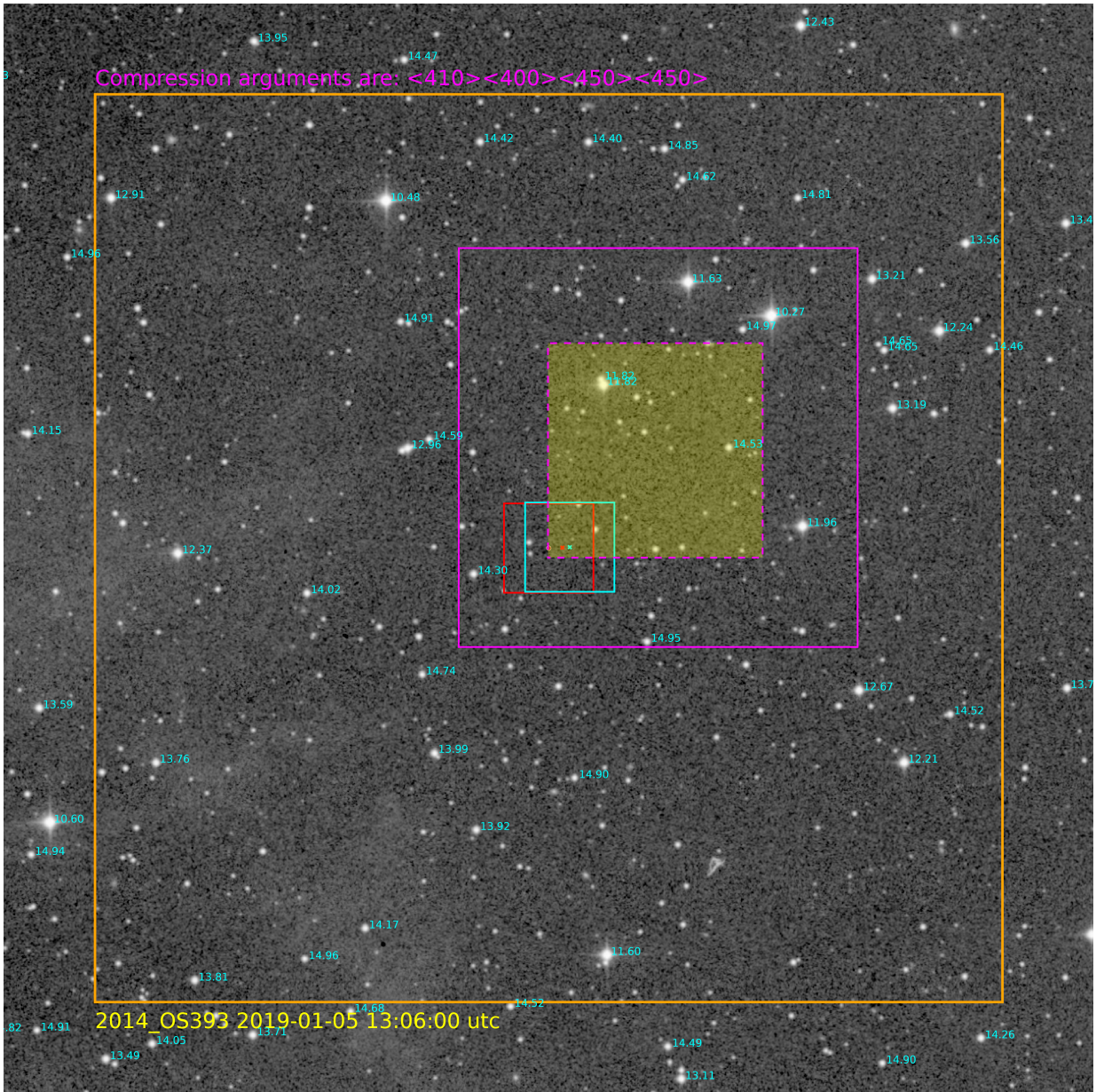


**Figure 2.** Window selection details for one set (REQID=131ss) of observations of OS<sub>393</sub>. The background image is taken from the Palomar Digital Sky Survey (red filter, second generation reduction); celestial north points straight down and celestial east points to the right. The orange box is the LORRI FOV with  $X_{\text{LORRI}}$  (the direction of increasing CCD columns) pointing to the right and  $Y_{\text{LORRI}}$  (the direction of increasing CCD rows) pointing up. The magenta box is the requested window (i.e., the window specified by the command arguments listed in magenta just above the orange box). The dashed magenta box (with light yellow background highlighting) is the magenta box reduced by the size of the pointing deadband ( $500 \mu\text{rad} = 104''$ ) in each dimension. We generally sized the image windows to capture both the KBO and at least one star with  $V \leq 13$  within the dashed magenta box. The red dot gives the LORRI boresight location, which is where the pointing control system commanded OS<sub>393</sub> to be placed. The red X shows the size of the pointing deadband centered on the LORRI boresight. The red X shows the predicted OS<sub>393</sub> location using the ephemeris used in planning the observations, which is offset from the boresight by the absolute pointing error derived using astrometry from  $4 \times 4$  images taken near the time of the  $1 \times 1$  observations. The cyan X shows the predicted OS<sub>393</sub> location using the new ephemeris generated based on the location of OS<sub>393</sub> in the  $4 \times 4$  images. The cyan box is the pointing deadband centered on that location. The  $V$  magnitudes from APASS for stars in the UCAC4 catalog are indicated in cyan.

**Table 2.** *New Horizons* KBO High Resolution Observations

Target	Dynamical Class	REQID	MET Range	Obs Date (UTC)	$r$ (au)	$\Delta$ (au)	Phase (deg)	SEA (deg)	Res (km)
2011 HK <sub>103</sub>	SD	123u	396814919–396815043	2018-08-17 12:30:01–12:32:05	42.36	0.290	50.6	129.1	215
		123v	396815819–396815943	2018-08-17 12:45:02–12:47:05					
		123w	397013099–397013223	2018-08-19 19:33:01–19:35:05	42.35	0.280	54.1	125.6	208
		123x	396815819–396815943	2018-08-19 19:48:01–19:50:05					
2011 JY <sub>31</sub>	CC	126oo	398776019–398776143	2018-09-09 05:15:01–05:17:05	42.44	0.154	57.9	121.9	114
		126pp	398776919–398777043	2018-09-09 05:30:01–05:32:05					
		126qq	398986019–398986143	2018-09-11 15:35:01–15:37:05	42.44	0.145	64.8	115.0	108
		126rr	398986919–398987043	2018-09-11 15:50:01–15:52:05					
2011 HZ <sub>102</sub>	CC	129qq	405876104–405876228	2018-11-30 09:29:46–09:31:50	43.15	0.185	47.1	132.7	137
		129rr	405876494–405876618	2018-11-30 09:36:16–09:38:20					
		129ss	406219919–406220043	2018-12-04 09:00:01–09:02:05	43.15	0.168	56.0	123.8	125
		129tt	406220309–406220433	2018-12-04 09:06:31–09:08:35					
2014 OS <sub>393</sub>	CC	131ss	408999419–408999543	2019-01-05 13:05:01–13:07:05	43.33	0.0918	81.9	98.0	68.2
		131tt	408999824–408999948	2019-01-05 13:11:46–13:13:50					
		131qq	409067559–409067683	2019-01-06 08:00:41–08:02:45	43.33	0.0922	85.9	94.0	68.5
		131rr	409067954–409068078	2019-01-06 08:07:16–08:09:20					
2014 PN <sub>70</sub>	CC	132v	414396119–414396243	2019-03-09 00:10:01–00:12:05	43.89	0.139	59.6	120.2	103
		132w	414396719–414396843	2019-03-09 00:20:01–00:22:05					
		132x	414568919–414569043	2019-03-11 00:10:01–00:12:05	43.89	0.129	65.4	114.5	95.8
		132y	414569519–414569643	2019-03-11 00:20:01–00:22:05					

NOTE—“Target” is the IAU KBO designation. “Dynamical Class” refers to the KBO dynamical class: “CC” is short for “cold classical” and “SD” is short for “scattered disk”. “REQID” is one of the FITS keywords for LORRI images used as a target identifier; for the actual FITS keywords, the REQIDs listed here are preceded with KALR\_HK103\_, KALR\_JY31\_, KALR\_HZ102\_, KALR\_OS393\_, and K2LR\_PN70\_ for the KBOs in this program. “MET” stands for Mission Elapsed Time and is used for spacecraft timekeeping. “Obs Date” values are universal coordinated time (UTC) values for the mid-times of the first and last images in the relevant sequence in the spacecraft frame. “ $r$ ” is the target’s heliocentric distance. “ $\Delta$ ” is the target’s distance from the spacecraft. “Phase” is to the sun-target-spacecraft angle (solar phase angle). “SEA” is the sun-spacecraft-target angle (solar elongation angle). “Res” is the projected distance in kilometers subtended by 1 LORRI pixel at the KBO. The actual spatial resolution at the KBO is approximately two LORRI pixels.

### 3. KBO PHOTOMETRY

We performed aperture photometry on all the LORRI  $1\times 1$  images (Table 3). In all cases, we used a 5-pixel radius circular aperture to measure the signal from the KBO, and we subtracted a background level derived from the mode of the signal contained within an annulus with inner radius of 10 pixels and outer radius of 20 pixels. The error in the net signal was calculated in the standard way, accounting for both the photon statistics of the KBO signal and the variation of the signal in the background region. The measured signals include contributions from both components of the binaries discussed in the next section.

We converted LORRI signal rates to standard  $V$  magnitudes in the Johnson photometric system using:

$$V = -2.5 \log(S/t_{\text{exp}}) + \text{ZPT} + \text{COLOR} - \text{AC} \quad (1)$$

where  $V$  is the magnitude in the standard Johnson  $V$  band (i.e., specifies the target’s flux at  $5500 \text{ \AA}$ ),  $S$  is the measured signal in the selected photometric aperture (DN),  $t_{\text{exp}}$  is the exposure time (0.5 s for all the images in this program), ZPT is the photometric zero point (18.78 for  $1\times 1$  LORRI images), COLOR is a color correction term of 0.067 assuming an Arrokoth-like color (Grundy et al. 2020) for all the KBOs, and AC is an aperture correction term to convert from the flux collected in a specified synthetic aperture to the total flux integrated over the LORRI PSF (0.1 was used here).

The two independent measurements on the same day are generally consistent (i.e., equal to each other within their  $1\sigma$  errors). However, several of the objects show significant changes in brightness from one observation date to the other, indicating substantial lightcurve variations over that time. More extensive lightcurve measurements for two of these KBOs (HK<sub>103</sub> and JY<sub>31</sub>) were obtained as part of the LORRI  $4\times 4$  program (Verbiscer et al. 2019), and the  $V$ -mag values reported here are consistent with those reported for the  $4\times 4$  program.



**Table 3.** *New Horizons* KBO Photometry

Target	REQID	Signal (DN)	$V$
2011 HK <sub>103</sub>	123u	$9.94 \pm 1.01$	$15.59 \pm 0.11$
	123v	$8.95 \pm 0.96$	$15.71 \pm 0.12$
	123uv	$9.40 \pm 0.90$	$15.65 \pm 0.10$
	123w	$8.29 \pm 1.18$	$15.79 \pm 0.15$
	123x	$8.36 \pm 0.96$	$15.78 \pm 0.12$
	123wx	$8.39 \pm 0.84$	$15.78 \pm 0.11$
2011 JY <sub>31</sub>	126oo	$27.62 \pm 1.486$	$14.48 \pm 0.058$
	126pp	$25.00 \pm 1.278$	$14.59 \pm 0.055$
	126oopp	$25.75 \pm 1.231$	$14.56 \pm 0.052$
	126qq	$21.53 \pm 1.432$	$14.75 \pm 0.072$
	126rr	$23.59 \pm 1.423$	$14.65 \pm 0.065$
	126qrr	$21.45 \pm 1.240$	$14.76 \pm 0.063$
2011 HZ <sub>102</sub>	129qq	$9.52 \pm 1.15$	$15.64 \pm 0.13$
	129rr	$9.05 \pm 1.02$	$15.69 \pm 0.12$
	129qrr	$9.15 \pm 0.93$	$15.68 \pm 0.11$
	129ss	$6.60 \pm 0.92$	$16.94 \pm 0.15$
	129tt	$4.08 \pm 0.87$	$16.56 \pm 0.23$
	129sstt	$5.36 \pm 0.72$	$16.26 \pm 0.15$
2014 OS <sub>393</sub>	131ss	$5.78 \pm 1.01$	$16.18 \pm 0.19$
	131tt	$5.39 \pm 0.99$	$16.26 \pm 0.20$
	131sstt	$5.77 \pm 0.81$	$16.18 \pm 0.15$
	131qq	$\leq 2.4$	$\geq 17.13$
	131rr	$\leq 2.1$	$\geq 17.28$
	131qrr	$\leq 1.5$	$\geq 17.57$
2014 PN <sub>70</sub>	132v	$2.67 \pm 1.22$	$17.02 \pm 0.50$
	132w	$3.72 \pm 1.19$	$16.66 \pm 0.35$
	132vw	$3.19 \pm 0.86$	$16.83 \pm 0.29$
	132x	$2.54 \pm 0.97$	$17.07 \pm 0.41$
	132y	$2.15 \pm 0.91$	$17.25 \pm 0.46$
	132xy	$2.49 \pm 0.71$	$17.09 \pm 0.31$

NOTE—“Target” is the IAU KBO designation. “REQID” is one of the FITS keywords for LORRI images used as a target identifier, as previously explained. In addition to presenting data from composite images for a single REQID, we also include data from composite images produced by combining all the images from two REQIDs that were taken back-to-back on the same day. OS<sub>393</sub> was not detected in REQIDs 131qq and 131rr, and we give  $3\sigma$  upper limits in those cases. “Signal” is the total measured signal within a 5-pixel radius aperture centered on the target and its  $1\sigma$  uncertainty. We adopted an aperture correction term of 0.10 to convert from flux within a 5-pixel radius to flux within an infinite aperture. “ $V$ ” is the target’s  $V$ -mag and its uncertainty, assuming the target has a spectral energy distribution similar to that of KBO Arrokoth. (HK<sub>103</sub> is an SD, not a CC like Arrokoth, so the color correction in this case might not be as accurate as for the other objects.)

## 4. SEARCHES FOR BINARIES

### 4.1. KBO Composite Images

To achieve the sensitivity required to detect the targeted KBOs in LORRI  $1\times 1$  format, we created composite images by combining the 125 images taken for each REQID. We also created composites by combining all 250 images for the two REQIDs taken on the same day to improve the SNR even further and produce the deepest imaging possible for each KBO on a given date.

The fastest apparent (non-sidereal) motion of the KBOs was  $\sim 0''.2 \text{ s}^{-1}$ , which means the KBO moved by  $\leq 0.1$  pixel relative to the stars in a single 500 ms exposure. Thus, the KBO-to-star relative motion is negligible for a single LORRI  $1\times 1$  image. However, the KBOs moved by up to  $\sim 26$  pixels relative to the stars over the full time duration needed to obtain the 125 images in a single REQID. This KBO-to-star relative motion must be taken into account when producing composite images. The pointing drift within the ACS deadband described earlier must also be taken into account when producing composite images.

For this program we produced two types of composite images: one set co-aligned on the KBOs (using the KBO ephemeris to account for the KBO-to-star apparent motion; this smears the stars in the field) and another set co-aligned on the stars detected in the images (this smears the KBOs). Before co-adding the images, we first remove any residual background light by subtracting linear fits to the background level, first row-by-row then column-by-column. The former removes systematic sub-DN level horizontal structure in the LORRI images, while the latter removes the “jailbars” pattern sometimes seen in LORRI images (cf., [Weaver et al. 2020](#)). We use the World Coordinate System (WCS) keywords, which were calculated using astrometric solutions with the Gaia catalog stars detected in each image, to determine the appropriate shifts to apply when combining all the images. To mitigate the effects of pixel outliers (e.g., pixels affected by cosmic rays), we employ a robust averaging process to produce the composite images. Briefly, the pixel values for a stack at a particular (x,y) CCD location are compared to their median, and pixels are rejected if their values differ by more than  $\pm 3\sigma$  from their median, where  $\sigma$  is computed from a noise model for the LORRI CCD, which includes the Poisson noise from detected photons, CCD read noise, and noise in the CCD flat field. Note that this technique also suppresses the brightness of the smeared stars in the target-aligned stacks. We compare the image of the KBO in its target-aligned composite to the images of stars in the star-aligned composite to determine whether there is evidence for KBO binarity.

Here we present composite images that show both  $512 \times 512$  pixel regions centered on the windowed portion of the CCD and  $64 \times 64$  pixel regions centered on the KBO and a nearby star of comparable brightness. Careful examination of these composite images (the grey-scale figures displayed below for all five KBOs) can be used to determine the quality of the KBO detections and also provide a qualitative assessment of the evidence for KBO binarity.

A more quantitative assessment of KBO binarity was performed by fitting PSFs to the data. An independent image stacking technique similar to, but different from, the method described above was used to create double-sampled composite images for each of the REQIDs.<sup>4</sup> An empirical LORRI PSF derived from multiple images of calibration star fields, and which has remained stable over the entire

<sup>4</sup> See [Porter et al. \(2022\)](#) for the details on this technique as applied to the  $4\times 4$  images; essentially the same technique is applied here for the  $1\times 1$  images.

course of the *New Horizons* mission (Weaver et al. 2020), was used to perform an initial fit to the composite KBO images. For each stack of 125 images, we fit a model PSF by allowing it to shift in (X,Y), and multiplied by a scaling factor, to minimize a  $\chi^2$  estimate as the sum of the square of the difference between the model and real images. If the KBO were single, the difference image should look approximately like random noise. Binary KBO images would show systematic deviations in the difference images that are larger than expected from random noise. As discussed further below, the composite images of JY<sub>31</sub> and the composite image from the first epoch of OS<sub>393</sub> were not fit very well with single PSF solutions. Indeed, single PSF solutions for both JY<sub>31</sub> and OS<sub>393</sub> (Fig. 6 and Fig. 11) produced residual images that appeared to be over-subtracted in the center and under-subtracted at two points just outside the center. This is a clear signature of the KBOs appearing as two blended PSFs with just enough separation to be resolved.

Recognizing these deficiencies in the single-PSF solutions, we repeated the estimation procedure, but with two PSFs in the model rather than one. The two PSFs were required to be within 20 re-projected pixels ( $\approx 10''$ ) of each other and have positive flux values. For the KBOs that appeared to be single (especially HK<sub>103</sub> and HZ<sub>102</sub>), the two-PSF solutions favored keeping the two PSFs on top of each other, and then splitting flux between them. These solutions thus had effectively the same  $\chi^2$  for both single and double PSFs (see Fig. 4 and Fig. 8). However, the double PSF solutions for JY<sub>31</sub> and for the bright epoch of OS<sub>393</sub> were best fit with two well-separated PSFs of similar flux (Fig. 6 and Fig. 11). For JY<sub>31</sub> in particular, the differences between the single and double PSF residuals in Figure 6 are striking. The differences between the residuals for one and two PSFs are less noticeable for OS<sub>393</sub>, as it has both a lower SNR than JY<sub>31</sub> (5 vs 20) and is elongated in the same direction as the LORRI PSF. As discussed further below, OS<sub>393</sub> is not visible at all in the second epoch because it was near the dimmest point of its rotational lightcurve. The case of PN<sub>70</sub> is generally similar to those HK<sub>103</sub> and HZ<sub>102</sub>, but PN<sub>70</sub>'s lower SNR (3 vs 10) makes discrimination between the single-PSF and double-PSF problematic.

Both single PSF and double PSF fits to the composite images were attempted for each of the KBOs, which are discussed in turn below. In each case, we show  $20 \times 20$  double-sampled images centered on the KBO (i.e.,  $10 \times 10$  native pixels) and use false-color intensity maps to bring out features more clearly.

#### 4.2. SD 2011 HK<sub>103</sub>

SD KBO HK<sub>103</sub> is relatively bright and could be easily detected in each of the four composite images (Fig. 3). The composite images of HK<sub>103</sub> are slightly elongated, but so are the images of nearby stars and the PSF fitting procedure (Fig. 4) does not provide convincing evidence for binarity. Thus, we do not claim that HK<sub>103</sub> is binary based on the *New Horizons*  $1 \times 1$  data. *HST* observations of HK<sub>103</sub> also did not show any direct evidence of binarity (Benecchi et al. 2019), albeit at  $\sim 10 \times$  poorer spatial resolution than provided by the *New Horizons* program. The light curves of HK<sub>103</sub> at multiple solar phase angles derived from LORRI  $4 \times 4$  data (Verbiscer et al. 2019) reveal a relatively short rotational period (10.83012 h) with an amplitude that varies from 0.2 mag at a phase angle of  $51^\circ$  to 0.9 mag at a phase angle of  $96^\circ$  and do not show any evidence of binarity.

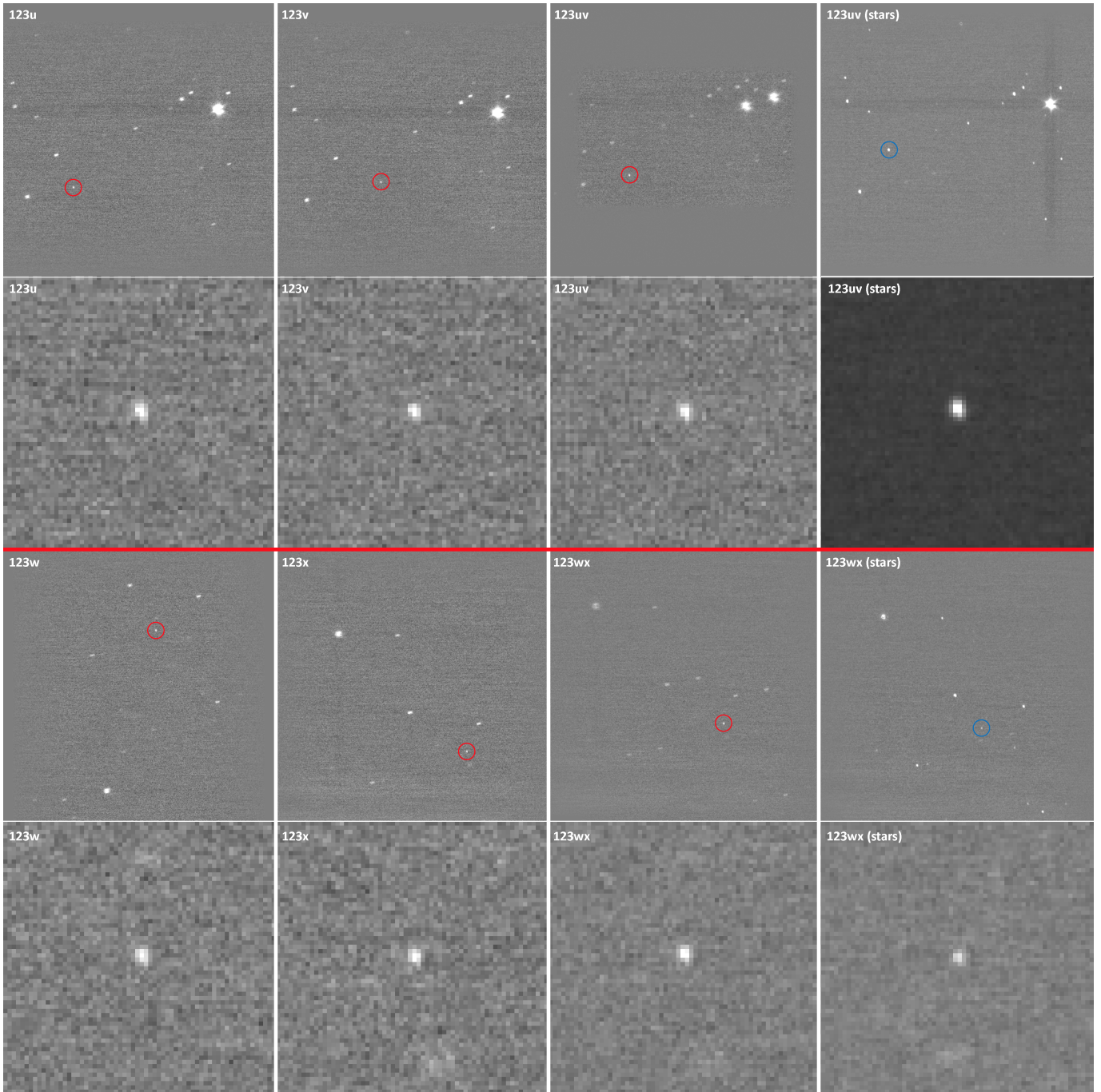


**Figure 3.** Composite images of  $HK_{103}$  from two different epochs (2018-08-17 above the red line and 2018-08-19 below the red line) are displayed. For each epoch, the top row shows  $512 \times 512$  frames containing the windowed portions of the full  $1024 \times 1024$  LORRI  $1 \times 1$  images, and the bottom row shows  $64 \times 64$  frames centered on either the KBO (circled in red in the top row) or a nearby star of comparable brightness (circled in blue in the top row). Composite images produced by co-aligning the images on the ephemeris locations of  $HK_{103}$  are displayed in the first three columns: 125 images are combined for the first two columns and 250 images are combined for the third column. The REQIDs are displayed in the upper left of each frame. Composite images created by co-aligning on stars for all 250 images are displayed in the fourth column. All images are displayed using a linear stretch ranging from  $-1$  to  $1$  DN, except for the top two images in the fourth column, which use a stretch from  $-2$  to  $4$  DN to avoid saturating the circled star. Celestial north points down and east points to the right in all images.

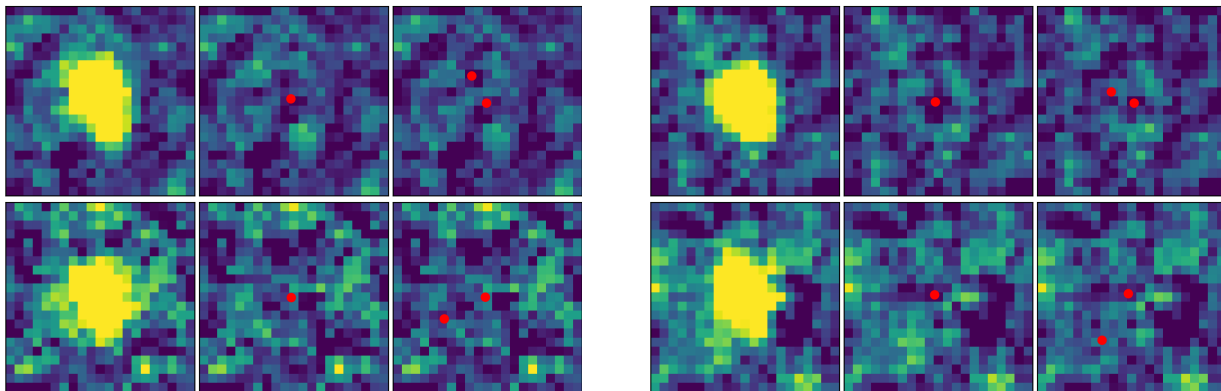


**Figure 4.** Single and double PSF fits to the double-sampled LORRI images of  $\text{HK}_{103}$ . The pair of panels on the left hand side shows the two observations from the first epoch (REQIDs 123u and 123v), and the pair of panels on the right hand side shows the two observations from the second epoch (REQIDs 123w and 123x). For the three frames within each observation epoch, the leftmost image shows the WCS-driven shift stack of the 125 images, the middle image shows the residuals after subtracting a best-fit single PSF, and the rightmost images show the residuals after subtracting the best-fit double-PSFs. The red dots show the locations of the center of each PSF fit. The same linear stretch is used for each image. Since the residuals in the double PSF solution look similar to those in the single PSF solution, and the locations of the object locations in the double PSF solution varies over the image,  $\text{HK}_{103}$  does not appear to be a binary.

#### 4.3. *CC 2011 JY<sub>31</sub>*

$\text{CC KBO JY}_{31}$  is also relatively bright and was easily detected in each of the four composite images (Fig. 5). Close inspection of these images shows that  $\text{JY}_{31}$ 's appearance is broader than the PSF in all four cases. For both of the first two composite images (from REQIDs 126oo and 126pp),  $\text{JY}_{31}$  appears to be elongated along a diagonal direction. For both of the second two composite images (from REQIDs 126qq and 126rr), which were taken  $\sim 34$  h after the first pair,  $\text{JY}_{31}$  appears to be extended in the horizontal dimension relative to the PSF. These impressions are reinforced by the PSF fitting analysis (Fig. 6), which shows that the double PSF solution is clearly better than the single PSF solution. As discussed further in Section 4.7, these morphological features in the images of  $\text{JY}_{31}$  can be associated with the motion of two bodies in a compact binary system.

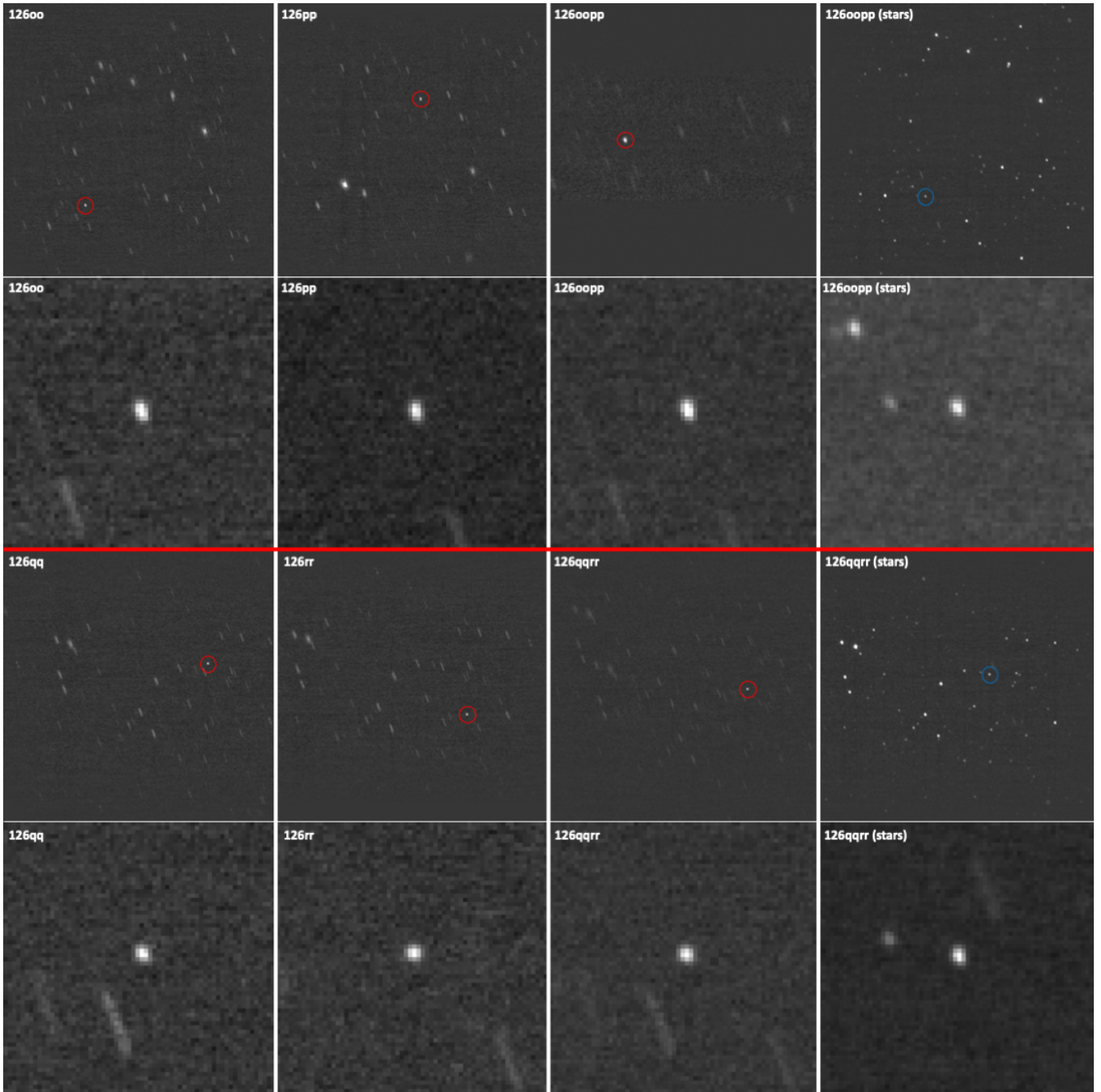


**Figure 5.** Composite images of  $JY_{31}$  from two different epochs (2018-09-05 above the red line and 2018-09-11 below the red line) are displayed. The layout is exactly as previously described for  $HK_{103}$ . In the first epoch of images co-aligned on the KBO's ephemeris,  $JY_{31}$  is clearly elongated in a diagonal direction relative to the stellar images. In the second epoch of images co-aligned on the KBO's ephemeris,  $JY_{31}$  appears to be broader horizontally relative to the stellar images. Thus, there is evidence for binarity for both epochs. All images are displayed using a linear stretch ranging from  $-1$  to  $2.5$  DN, except  $64 \times 64$  126pp and  $64 \times 64$  126qrrr (stars) are displayed on a linear scale from  $-1$  to  $3$  DN to avoid saturating on the brightest pixel and  $64 \times 64$  126oopp (stars) is displayed on a linear scale from  $-1$  to  $2$  DN to bring out the fainter stars. Celestial north points down and east points to the right in all images.

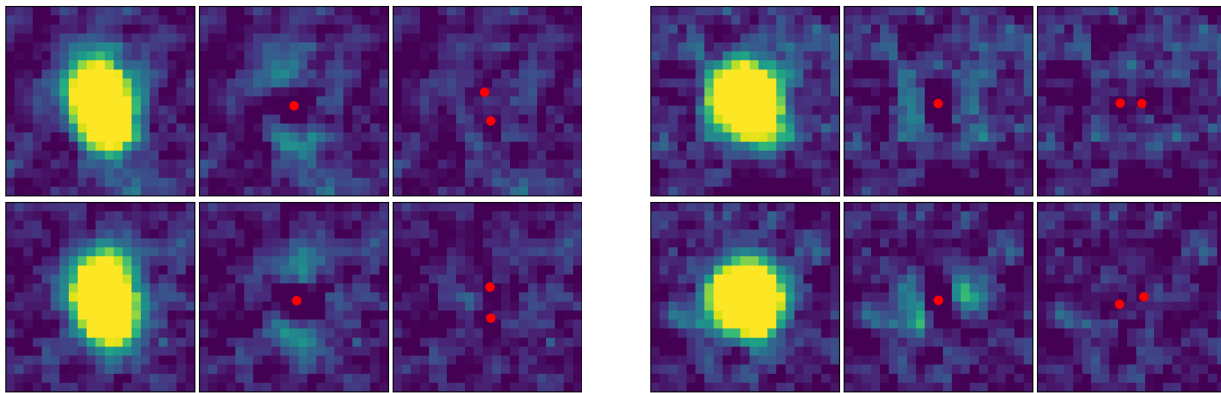


**Figure 6.** Single and double PSF fits to the double-sampled LORRI images of CC JY<sub>31</sub>. The pair of panels on the left hand side shows the two observations from the first epoch (REQIDs 126oo and 126pp), and the pair of panels on the right hand side shows the two observations from the second epoch (REQIDs 126qq and 126pp). See Figure 4 for detailed descriptions of each panel. Here, the double PSF solution is clearly much better than the single PSF solution, and the location of the two PSFs is consistent between the two observations in each epoch. The “high-low-high” residuals in the single PSF fits are typical of two barely resolved PSFs. We thus conclude that JY<sub>31</sub> is almost certainly a binary.

#### 4.4. *CC 2011 HZ<sub>102</sub>*

CC KBO HZ<sub>102</sub> has intermediate brightness and was clearly detected in each of the four composite images (Fig. 7). Close inspection of these images shows that HZ<sub>102</sub>’s appearance is stellar-like in all four cases, which suggests that HZ<sub>102</sub> is not a resolved binary system. This conclusion is supported by the more sophisticated PSF fitting analysis (Fig.8), which shows that the single and double PSF solutions have similar residuals.

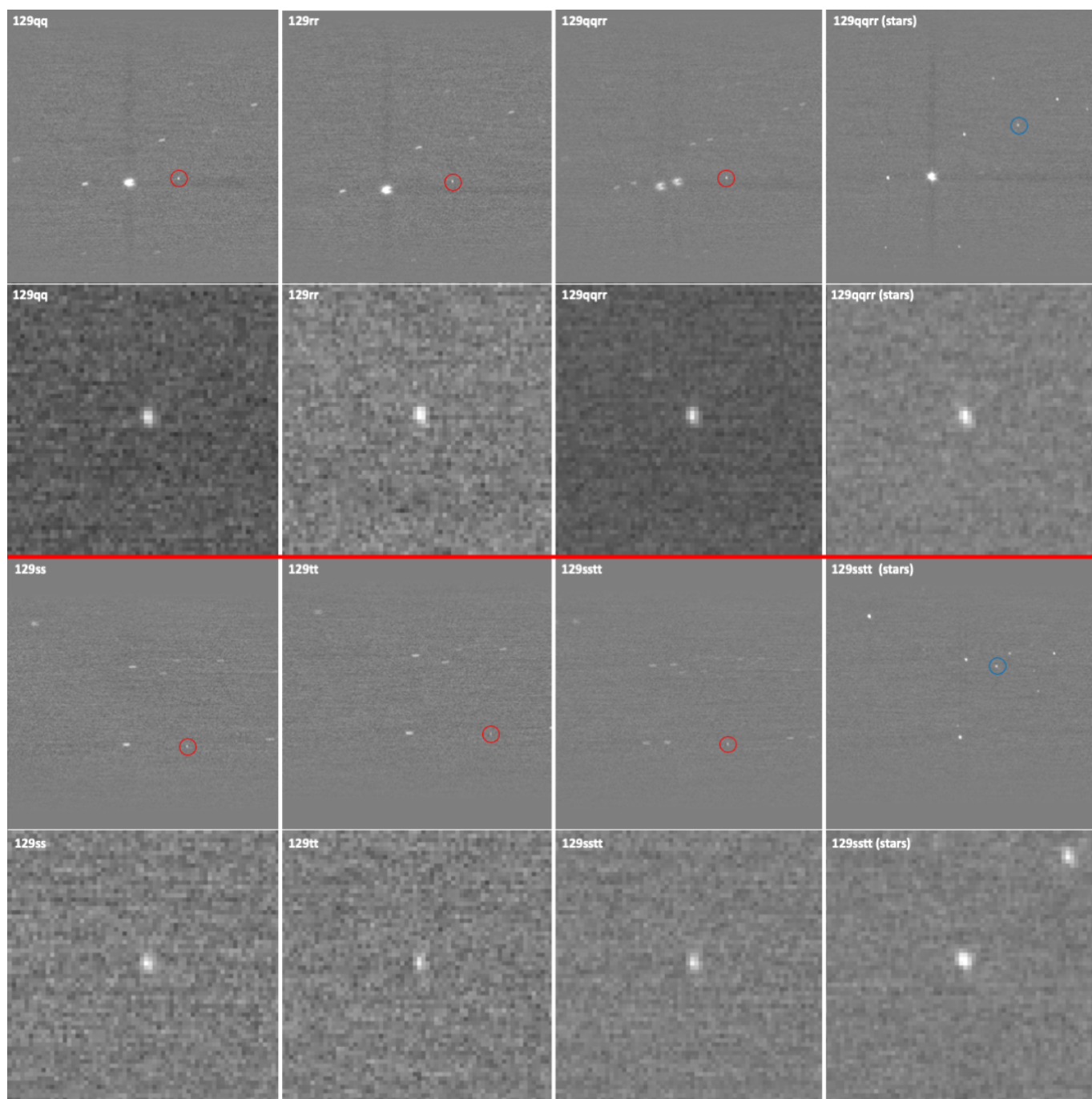


**Figure 7.** Composite images of  $\text{HZ}_{102}$  from two different epochs (2018-11-30 above the red line and 2018-12-04 below the red line) are displayed. The layout is exactly as previously described for  $\text{HK}_{103}$ . In all the composite images,  $\text{HZ}_{102}$  has a similar appearance to the PSF (i.e., to the stars), which shows there is no evidence for binarity in either epoch. All images are displayed using a linear stretch ranging from  $-1$  to  $1$  DN, except  $64 \times 64$  129qq and  $64 \times 64$  129qqr are displayed on a linear scale from  $-1$  to  $1.5$  DN to avoid saturating on the brightest pixel. Celestial north points down and east points to the right in all images.



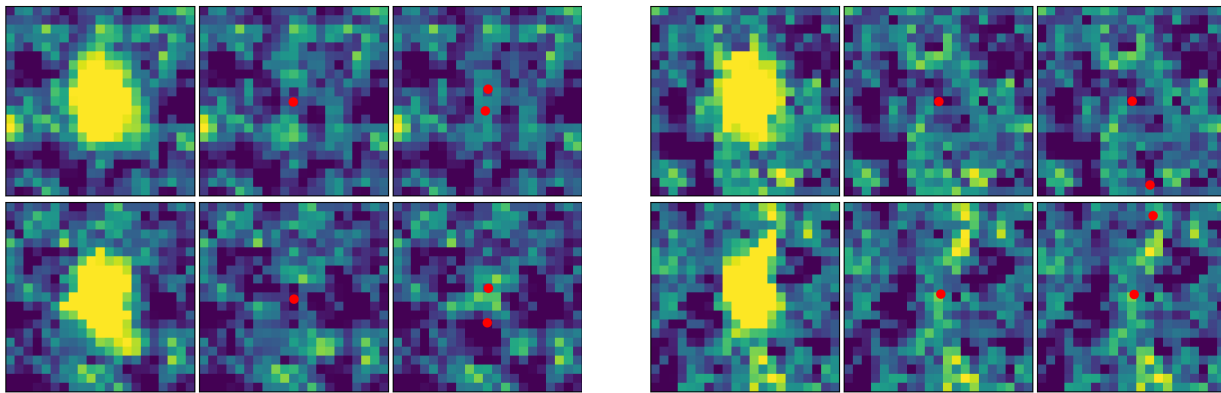


**Figure 8.** Single and double PSF fits to the double-sampled LORRI images of  $\text{HZ}_{102}$ . The pair of panels on the left hand side shows the two observations from the first epoch (REQIDs 129qq and 129rr), and the pair of panels on the right hand side shows the two observations from the second epoch (REQIDs 129ss and 129tt). See Figure 4 for detailed descriptions of each panel. Much like  $\text{HK}_{103}$ ,  $\text{HZ}_{102}$  is well-fit with a single PSF. While there is a consistency in the angle of the two PSFs in the first epoch, the dimmer second PSF flips sides relative to the primary PSF, and so is likely not real.

#### 4.5. *CC 2014 OS<sub>393</sub>*

In the first set of images of CC KBO  $\text{OS}_{393}$ , the object is detected with relatively poor SNR, and it is not detected at all in the second set (Fig. 9). We calculate SNR values of 5.7, 5.4, and 7.1 for REQIDs 131ss, 131tt, and their combination, respectively.

In the first set of images,  $\text{OS}_{393}$  appears to be more extended than for any of the other KBOs discussed here and is more extended than a similarly bright nearby star, providing evidence that  $\text{OS}_{393}$  is probably a binary system. If this interpretation is correct, the satellite is  $\sim 150$  km (2.24 pixels) from the primary at celestial position angle of  $\sim 207^\circ$ .

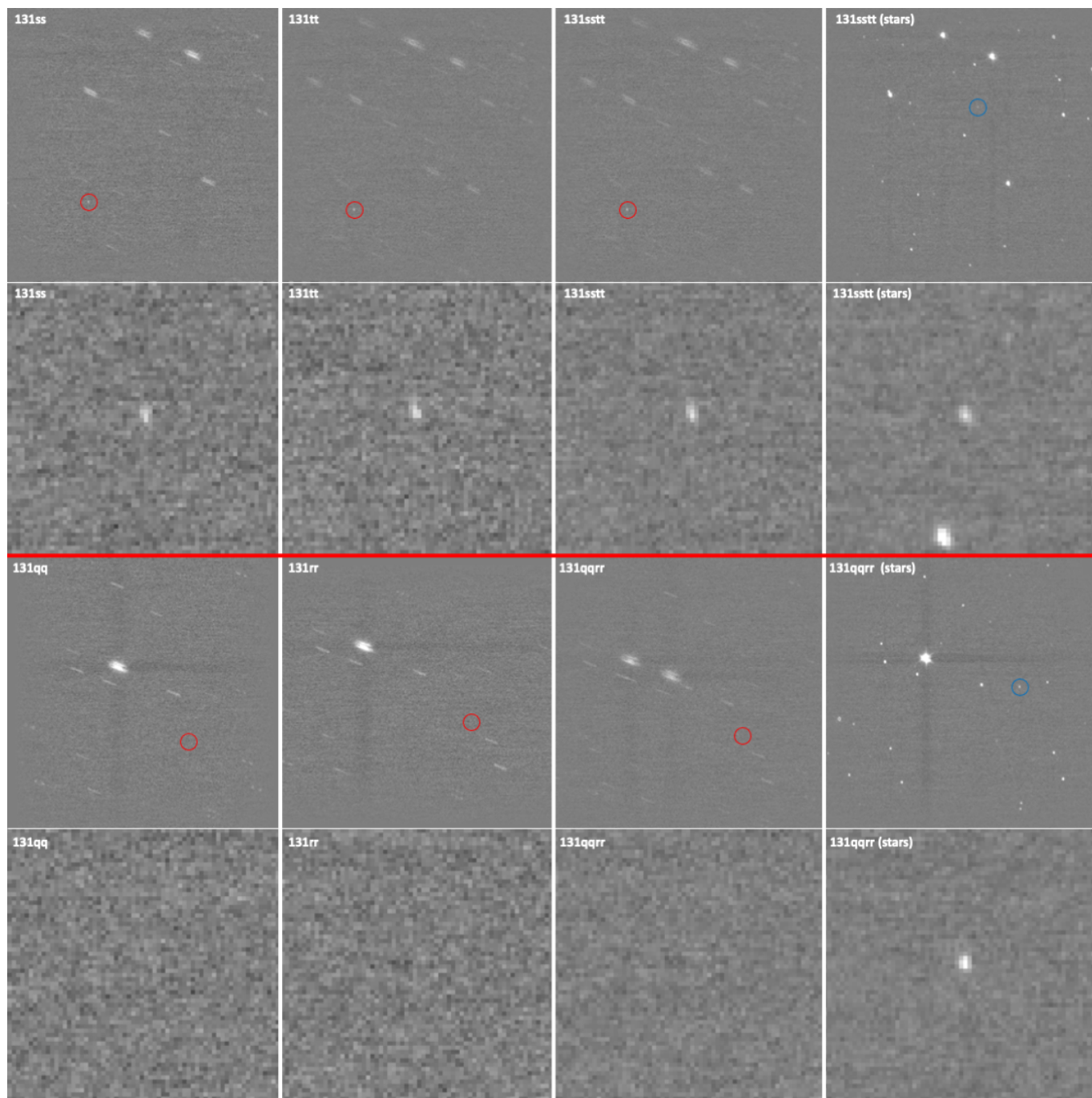


**Figure 9.** Composite images of OS<sub>393</sub> from two different epochs (2019-01-05 above the red line and 2019-01-06 below the red line) are displayed. The layout is exactly as previously described for HK<sub>103</sub>. OS<sub>393</sub> appears to be elongated relative to the expected PSF in the first epoch suggesting it is a binary object. Unfortunately, OS<sub>393</sub> could not be detected in the second epoch when it was near the minimum in its lightcurve brightness. All images are displayed using a linear stretch ranging from  $-1$  to  $1$  DN. Celestial north points down and east points to the right in all images.

Unfortunately, OS<sub>393</sub> wasn't detected in the second epoch (REQIDs 131qq and 131rr), probably because it was near its lightcurve minimum (see Fig. 10). We know that we searched in the correct location because the ephemeris for OS<sub>393</sub> is accurate to  $\sim 1$  pixel. Based on the photometry from the LORRI 4 $\times$ 4 program (Porter et al. 2022), we estimate that OS<sub>393</sub> was about two times fainter for the second epoch compared to the first, which pushed the object below our detection limit.

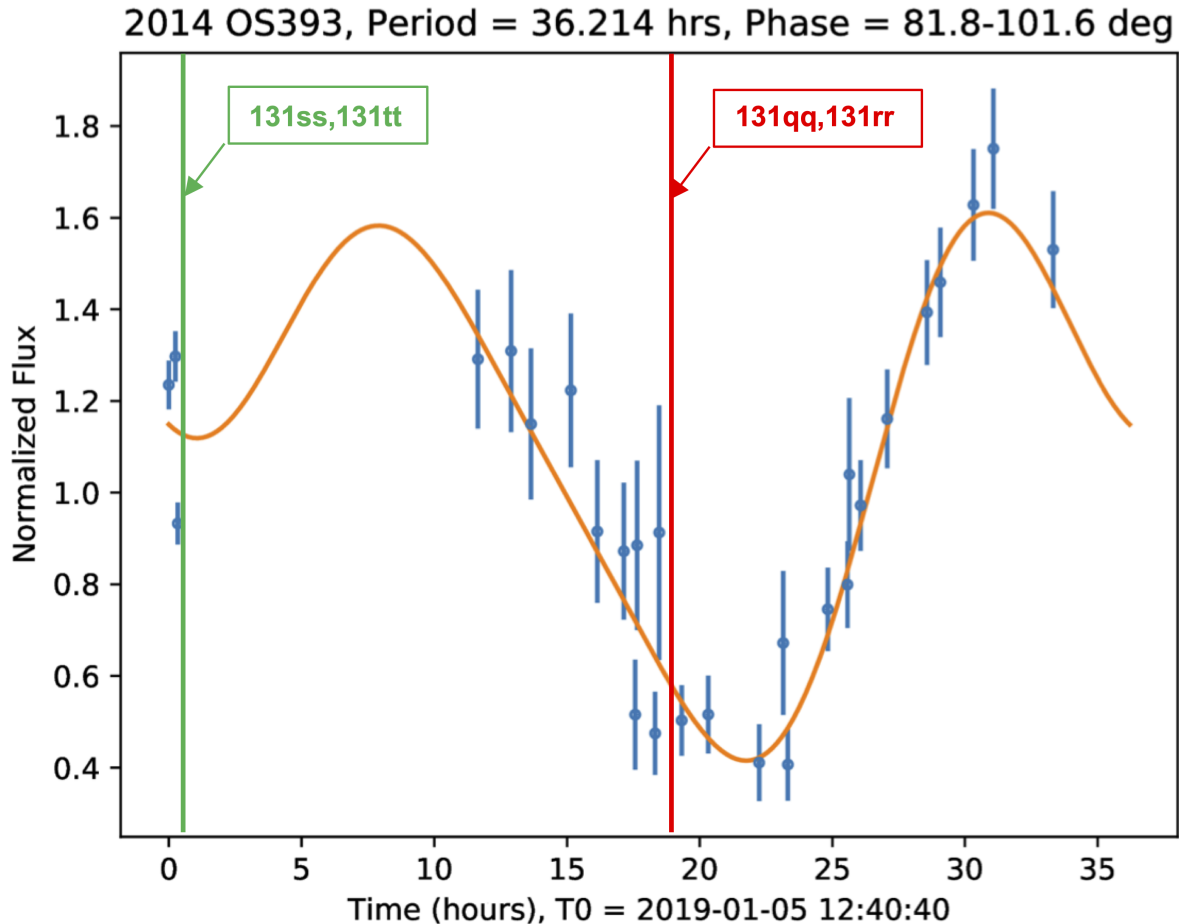


**Figure 10.** OS<sub>393</sub> lightcurve data from Porter et al. (2022) are plotted showing the strong variation of signal over time. The observation time for REQIDs 131ss and 131tt (green vertical line) occurred near the time of maximum brightness, whereas REQIDs 131qq and 131rr (red vertical line) were conducted near the time of minimum brightness.

Our PSF-fitting analysis of OS<sub>393</sub>'s images also suggests that this KBO is a binary (Fig. 11), but the low SNR in the first set of observations and the lack of a clear detection of the object in the second set make this conclusion more tentative than for JY<sub>31</sub>.

At Earth's distance from OS<sub>393</sub> during opposition ( $\sim 42$  au), the binary separation (if real) is only  $\sim 0''.005$ , which means imaging detection of the binary nature is unlikely with currently available facilities. OS<sub>393</sub> was discovered by *HST* but no direct evidence for binarity was seen in those images, which had a resolution of  $\sim 2400$  km (2 pixels, at  $0''.04$  per pixel). We note that the relatively long

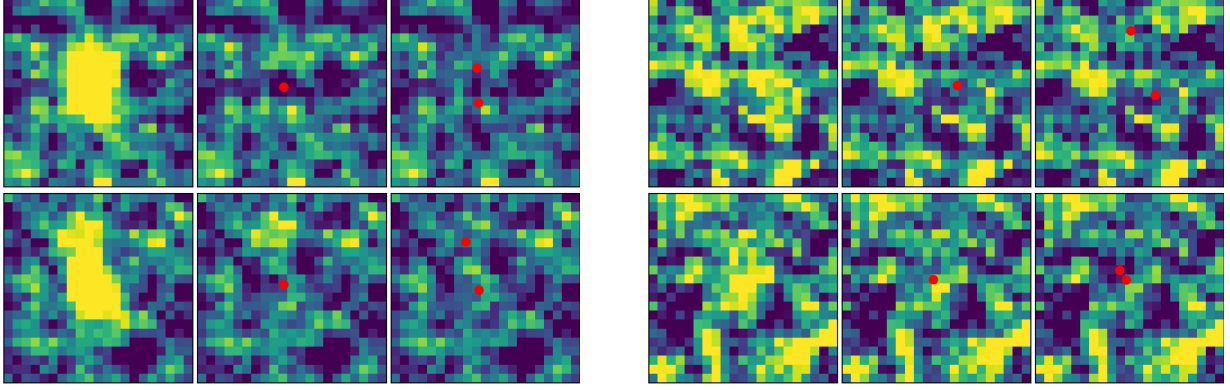


**Figure 11.** Single and double PSF fits to the double-sampled LORRI images of OS<sub>393</sub>. The pair of panels on the left hand side shows the two observations from the first epoch (REQIDs 131ss and 131tt), and the pair of panels on the right hand side shows the two observations from the second epoch (REQIDs 131qq and 131rr). See Figure 4 for detailed descriptions of each panel. The images of OS<sub>393</sub> in the first epoch appear to be elongated. Moreover, the locations of the PSFs in the double PSF solutions are roughly consistent in the two separate image sets taken in the first epoch. However, OS<sub>393</sub> is not visible at all in the second epoch. This is consistent with its lightcurve (see Fig. 10), which predicts that the KBO should be about one magnitude dimmer in the second epoch than the first.

lightcurve period ( $\sim 36$  h) is consistent with OS<sub>393</sub> being a tidally locked binary system. Perhaps precision lightcurve photometry, or occultation measurements (Porter et al. 2022), can shed further light on the possible binary nature of OS<sub>393</sub>.

#### 4.6. CC 2014 PN<sub>70</sub>

Unlike all the other cases considered here, CC PN<sub>70</sub> was not always in the windowed region of the CCD. For REQIDs 132v, 132w, 132x, and 132y, PN<sub>70</sub> was in 55, 52, 76, and 88 images, respectively, out of the total of 125 images in each case. As previously mentioned, the PN<sub>70</sub> background field was relatively sparse, which made it problematic to design a window that contained both the KBO and at least one star brighter than  $V = 13$ . A compromise we made was to put the single bright star near one edge of the window and the KBO near another edge. Unfortunately, the KBO moved in and out of the windowed region as the LORRI boresight drifted within the specified deadband. We used the predicted ephemeris of PN<sub>70</sub> to find all the images when the KBO was within the window and also at least 5 pixels from the edge, and we created composites using only these “good” images (Fig. 12).

PN<sub>70</sub> was also exceptionally faint, essentially at the sensitivity limit of LORRI. The SNRs were 2.2, 3.1, and 3.7 for REQIDs 132v, 132w, and 132vw, respectively. (The image of PN<sub>70</sub> from 132w had an anomalously narrow PSF, which suggests it may have been affected by a weak cosmic ray event or a pixel with larger than typical dark current.) The SNRs were 2.6, 2.4, and 3.5 for REQIDs 132x, 132y, and 132xy, respectively. For all these latter cases, there are pixels of comparable brightness to the peak located near the ephemeris location of PN<sub>70</sub> that make photometry in this case especially difficult. The photometry (Table 3) gives  $V \approx 17$  for these latter observations. Given the poor SNR for the PN<sub>70</sub> observations, we cannot draw any definitive conclusions about its binarity. The same conclusion is reached by the more refined analysis (Fig. 13).

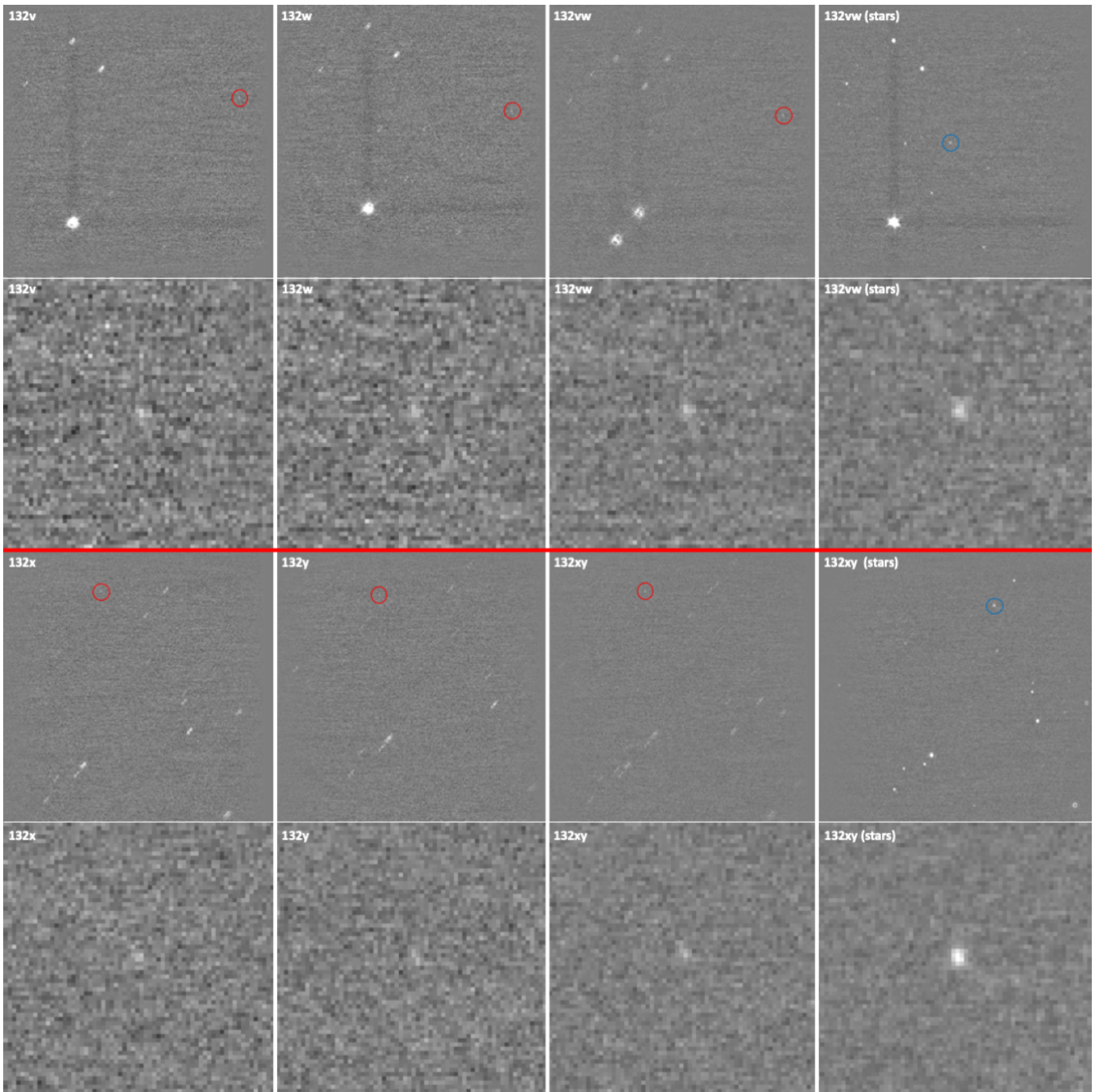


**Figure 12.** Composite images of PN<sub>70</sub> from two different epochs (2019-03-09 above the red line and 2019-03-11 below the red line) are displayed. The layout is exactly as previously described for HK<sub>103</sub>. PN<sub>70</sub> is detected in all these images but with low SNR. All images are displayed using a linear stretch ranging from  $-1$  to  $1$  DN. Celestial north points down and east points to the right in all images.

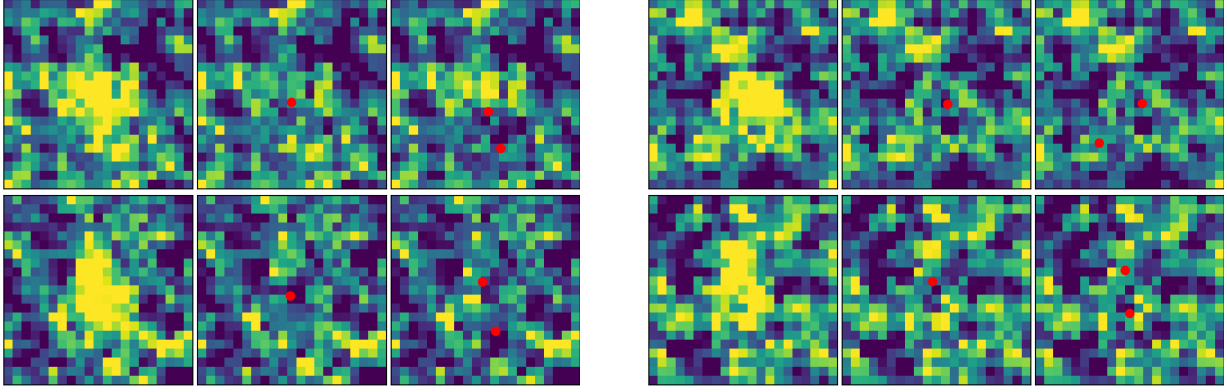


**Figure 13.** LORRI 1x1 observations for PN<sub>70</sub>. The pair of panels on the left hand side shows the two observations from the first epoch (REQIDs 132v and 132w), and the pair of panels on the right hand side shows the two observations from the second epoch (REQIDs 132x and 132u). See Figure 4 for detailed description. While PN<sub>70</sub> was detected in all four observations, it had a low SNRs in both epochs. In none of the observations was the two-PSF solution significantly better than the single PSF solution, which suggests there is no evidence that PN<sub>70</sub> is binary.

#### 4.7. Binary Orbit Determination of JY<sub>31</sub>

While JY<sub>31</sub> appears to be binary in both epochs, those observations alone are not sufficient to determine the orbital elements of the binary system. Each LORRI observation provides two data points, ( $\delta$ RA and  $\delta$ Dec), which means two observations can only provide four constraints. While we were able to extract a distinct astrometric point for each 125-image stack, for a total of four observations and eight constraints, they were close enough to each other ( $\sim 2\%$  of the orbit) that they were not effectively independent points. The high SNR of JY<sub>31</sub> in the LORRI 1 $\times$ 1 images meant that the uncertainty in the relative astrometry of the secondary with respect to the primary was small ( $\sim 0''.04$ ), or about 2-3% of the 1''.2-1''.7 apparent separation of the two bodies. A bound Keplerian orbit with an unknown system mass has seven free parameters, which can be described as the relative position/velocity state vector of the second with respect to the primary, plus the total system mass. Alternatively, the orbit can be parameterized as the system semimajor axis, eccentricity, longitude of the ascending node, argument of the periaapse, anomaly at epoch, and orbital period. If we constrain the mutual orbit to be circular, the eccentricity of the orbit is fixed at zero, and the argument of the periaapse becomes undefined (as there is no discrete periaapse). The number of free parameters for a circular orbit with unknown mass is therefore five, but a unique solution is still not possible with only two astrometric observations. While binary KBOs have been detected at a large range of mutual eccentricities (Grundy et al. 2019), all binary KBOs with a semimajor axis smaller than 3000 km have been found to have circular mutual orbits (Grundy et al. 2019), with the exception of (42355) Typhon-Echidna, which may have been perturbed by encounters with Neptune (Grundy et al. 2008). This result implies that these tight KBO orbits have been circularized by mutual body tides raised on the two objects (Porter & Grundy 2012). Since any plausible mutual orbits for JY<sub>31</sub> are smaller than this, we can reasonably assume that JY<sub>31</sub>'s binary has a circular orbit.

To test how constraining the eight-but-really-four parameters were on the circular solution space, we used *emcee* (Foreman-Mackey et al. 2013, 2019) to create a Markov chain Monte Carlo (MCMC) solution cloud, shown in Figure 14. There were a range of solutions that were consistent with a

roughly two day orbit, but the solutions were highly-correlated in semimajor axis and period, and the orbit pole was essentially unconstrained. The LORRI  $1\times 1$  resolved observations alone could therefore not be used to fit the mutual orbit of JY<sub>31</sub>.

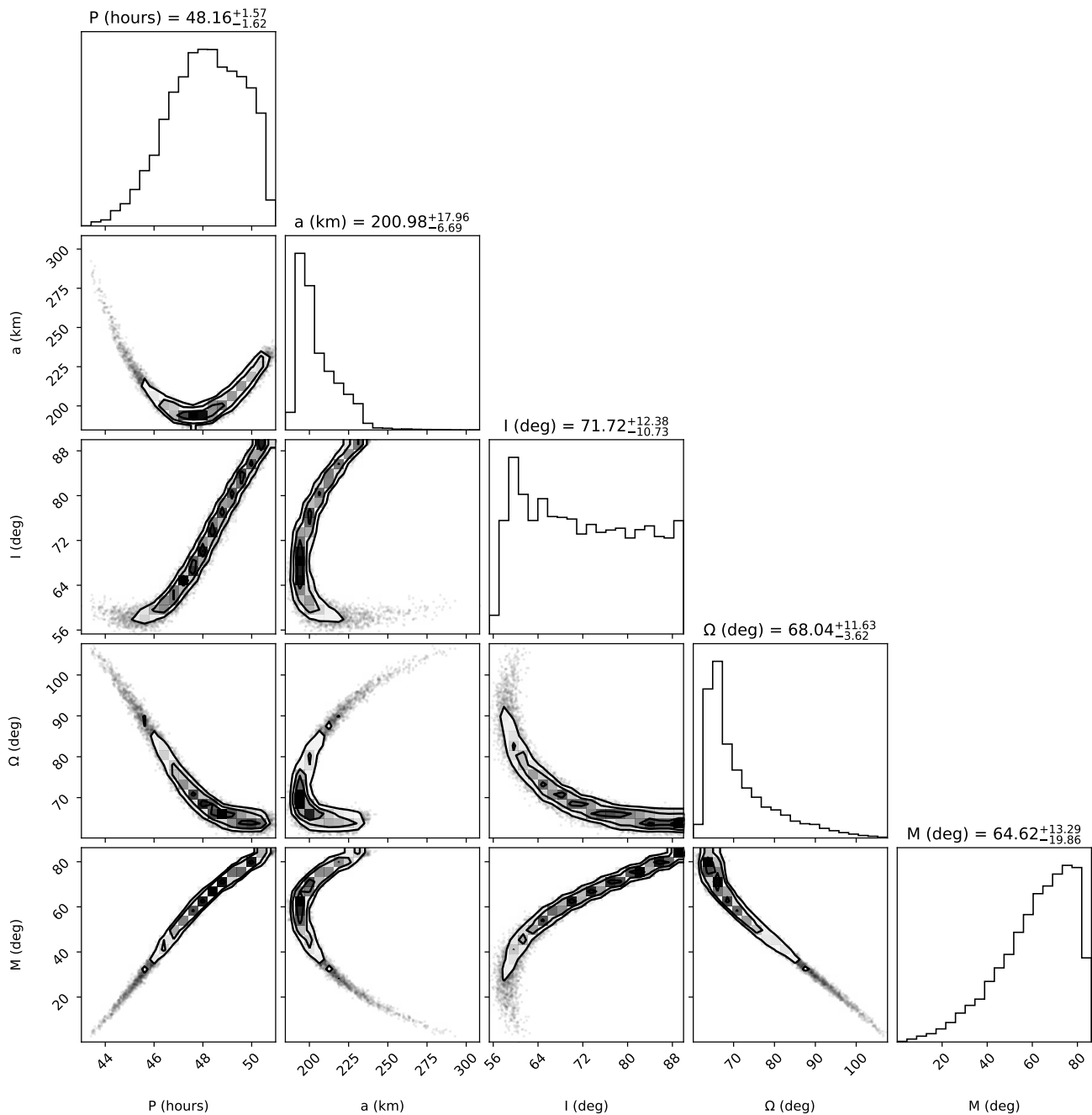


**Figure 14.** The probability distribution function (PDF) of the mutual orbit solution for JY<sub>31</sub>'s binary orbit using relative astrometry from the LORRI  $1\times 1$  images (see Fig. 6). The orbit is assumed to be circular, and the fit parameters are period, orbital radius, inclination, longitude of the ascending node, and mean anomaly at the epoch. For this solution, the period is unconstrained, which results in a wide spread in the fit parameters.

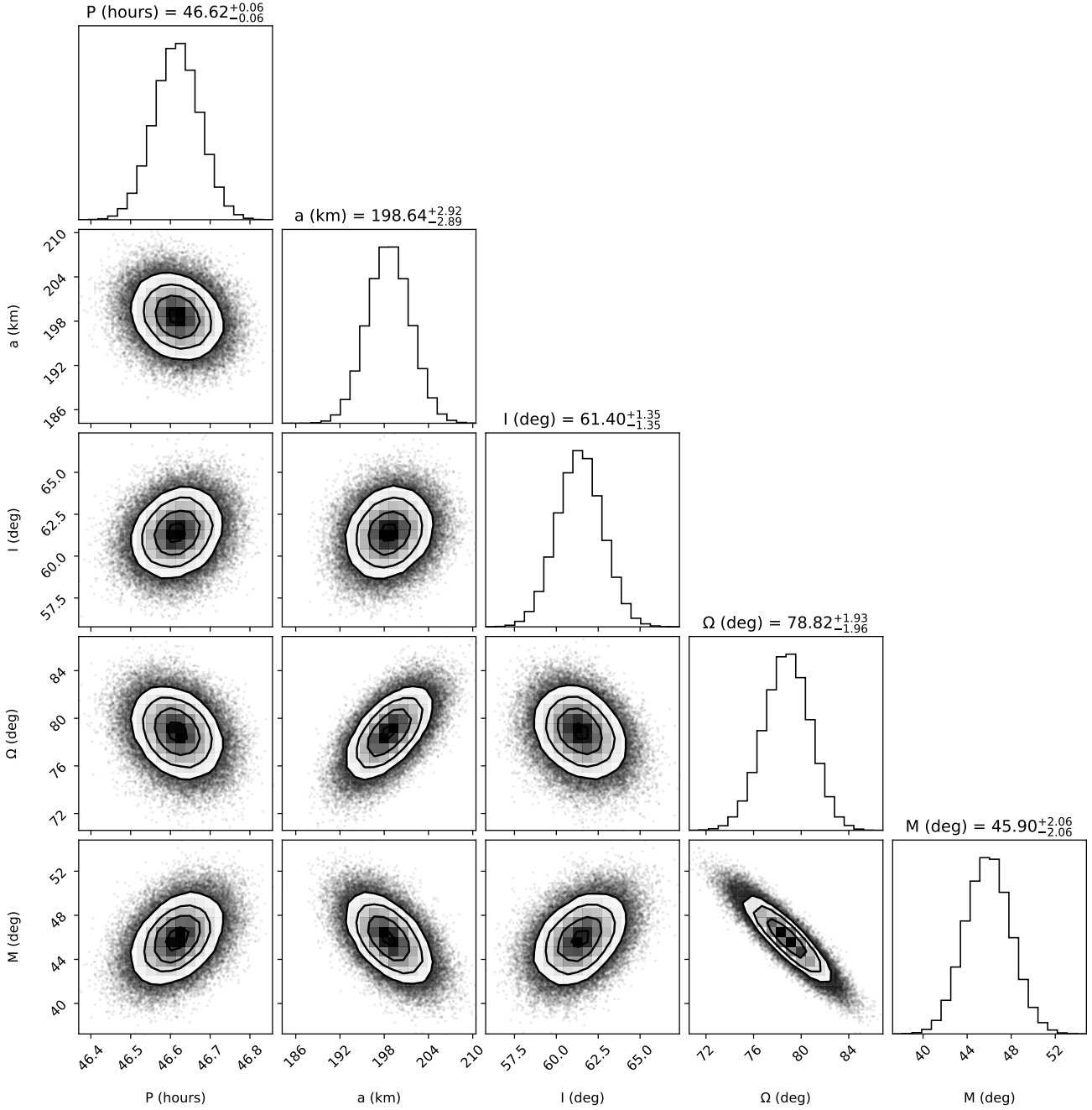


**Figure 15.** The same as for Fig. 14, except for this solution the period is constrained by the lightcurve results from the  $4\times 4$  data (Porter et al. 2022), which results in much tighter distributions of the fit parameters.

In addition to the LORRI  $1\times 1$  images, *New Horizons* also observed JY<sub>31</sub> in  $4\times 4$  format at five different epochs, with 18 observations spanning  $\sim 36$  h in each epoch, including observations just before and just after the  $1\times 1$  observations (Verbiscer et al. 2019). These observations allowed us to constrain the rotational period of JY<sub>31</sub> to be  $46.6 \pm 0.05$  h. Because the orbit is so tight, and because we had already assumed that it has tidally circularized, we made the further assumption that the two bodies of the JY<sub>31</sub> system are tidally locked, such that their rotation period is equal to their



**Table 4.** Orbital Elements of Binary Cold Classical KBO 2011 JY<sub>31</sub>

a	e	i	$\Omega$	M	P
(km)		(deg)	(deg)	(deg)	(hours)
$198.6 \pm 2.9$	0	$61.5 \pm 1.3$	$78.8 \pm 1.9$	$45.90 \pm 2.06$	$46.62 \pm 0.06$

NOTE—“a” is the semi-major axis of the binary orbit, “e” is the eccentricity, “i” is the inclination relative to the object’s heliocentric orbit pole, “ $\Omega$ ” is the longitude of the ascending node of the binary orbit, “M” is the mean anomaly at the epoch of observation, and “P” is the binary orbital period. The binary orbit’s inclination relative to the ICRF pole is  $61^{\circ}34 \pm 1^{\circ}34$ .

orbit period. If the orbit is indeed circular, this should be a reasonable assumption because Porter & Grundy (2012) found that tidal de-spinning to a double-synchronous configuration was very rapid after similar-sized binary KBOs achieved tidal circularization. The lightcurve itself also suggests tidal synchronization, as only the one period was evident in the solution, with no beat frequencies that might be expected from two objects rotating at different rates (Verbiscer et al. 2019; Porter et al. 2022). This result provided a fifth constraint on the five parameters, allowing us to determine a proper solution set for the mutual orbit. As shown in Figure 15, the combination of the LORRI lightcurve period constraint and the LORRI  $1 \times 1$  resolved astrometry was sufficient to provide an excellent constraint on the mutual orbit of JY<sub>31</sub>. We were able to constrain the semimajor axis of circular orbit to be  $198.6 \pm 2.9$  km and the inclination of the mutual orbit to be  $61^{\circ}34 \pm 1^{\circ}34$  to the ICRF pole, or  $61^{\circ}5 \pm 1^{\circ}3$  to JY<sub>31</sub>’s heliocentric orbit pole. While binary KBOs observed from Earth typically have a mirror-ambiguity that leads to two conjugate orbit pole solutions (Grundy et al. 2019), the *New Horizons* LORRI  $1 \times 1$  observations of JY<sub>31</sub> were  $7^{\circ}$  apart in solar phase angle. This, plus the “sense-of-motion” detectable within each day of data, was sufficient to break the degeneracy and constrain JY<sub>31</sub>’s mutual orbit to only one family of solutions. The orbital elements of JY<sub>31</sub> derived from our analysis are provided in Table 4.

With a physical separation of  $\sim 200$  km, JY<sub>31</sub>’s components are almost certainly tidally locked to each other. From the orbit, the total mass of the system is  $\sim 1.7 \times 10^{17}$  kg. If we assume each component has a density of  $500 \text{ kg/m}^3$ , similar to comet 67P/Churyumov-Gerasimenko (Jorda et al. 2016), and that the two components are roughly equal in size, then the two components would have equivalent radii of  $\sim 34$  km, making them at least 5.8 radii apart. If the bodies have a density of  $1000 \text{ kg m}^{-3}$ , their equivalent radii would be  $\sim 27$  km, putting them at least 7.4 radii apart. Tidal circularization occurs rapidly at separations less than 10 radii (Porter & Grundy 2012), and tidal locking occurs shortly thereafter.

The equivalent radii derived from the dynamical analysis are significantly larger than the values estimated from the visible photometry (see Table 1). The dynamical analysis suggests that *each* component of the JY<sub>31</sub> primary has an equivalent spherical diameter of at least 56 km, assuming they are less dense than water ice, whereas Table 1 suggests that their diameters should be  $\sim 42$  km, assuming the geometric albedo is 15% and the quoted visible magnitude is actually the sum of the

light from two equally bright objects. However, Porter et al. (2022) gives  $H_0 = 8.1$  for JY<sub>31</sub>, which raises the photometrically derived size up to  $\sim 58$  km for each component of the binary, fully consistent with the dynamically derived size.

## 5. DISCUSSION

In our small survey of KBOs passing close to the *New Horizons* spacecraft, we found that two out of four CCs are binary, while the single SD KBO searched does not appear to have a companion  $\geq 450$  km from the main object. One of the CCs searched (PN<sub>70</sub>) was too faint to draw definitive conclusions about its possible binarity, which essentially means that two of three CCs surveyed by *New Horizons* have companions.

The observational status of KBO binaries has been summarized in a recent review paper (Noll et al. 2020), which provides updates to an earlier review (Noll et al. 2008a). These reviews conclude that the binary fraction of SD KBOs is probably less than  $\sim 10\%$ , whereas at least 20% of KBO CCs are binaries. However, these papers acknowledge that the binary fraction estimates suffer from various selection effects that could bias the results, and at least make them highly uncertain.

Fraser et al. (2017a,b) discovered a sub-population of “blue” objects among the CCs, and they argued that essentially *all* of those objects must have been born as binaries. They hypothesized that these blue CC binaries must have formed near  $\sim 38$ -40 au and were subsequently pushed by gravitational interactions with Neptune into the CC region. These authors invoked the streaming instability to form rotating pebble clouds within the solar nebula, which subsequently produced larger planetesimals via gravitational collapse. According to their simulations, binary planetesimals are the predominant large bodies produced during this process, together with a large number of smaller single objects (the latter are needed to carry away the angular momentum of the original pebble cloud). The CCs surveyed by *New Horizons* all seem to be red (like most of the CC KBOs; Benecchi et al. (2019)), which means the high binary fraction for the blue CCs might not apply to the objects *New Horizons* surveyed.

However, a new paper (Nesvorný et al. 2021) addresses planetesimal formation in the CC region in detail and concludes that binary formation is likely to be predominant in this region, reinforcing their earlier arguments along the same lines (Nesvorný et al. 2019). These authors also invoke the streaming instability followed by gravitational collapse of pebble clouds as the primary planetesimal formation mechanism in the CC region, and they demonstrate that binaries naturally form for a wide range of pebble cloud angular momentum conditions. Thus, the high binary fraction for the CC KBOs surveyed by *New Horizons* is consistent with current CC KBO formation scenarios. Furthermore, the *New Horizons* results extend the previous surveys to smaller objects ( $H_0 = 5 - 8$  for the previous surveys versus  $H_0 = 8 - 10$  for *New Horizons*) and considerably smaller binary separations ( $\geq 2000$  km versus  $\sim 200$  km). As shown in Porter & Grundy (2012), the combination of Kozai-Lidov cycling and tidal friction (also known as KCTF) may have produced a large number of very tight binary KBOs, which is also consistent with the *New Horizons* detections.

The previous surveys showed that most of the CC binaries have orbits with small eccentricities (i.e., nearly circular orbits), nearly equal-size bodies, and tend to be relatively compact (i.e., with semi-major axes a small fraction of the mutual Hill sphere radius), which is also true for the two CC binaries discovered by *New Horizons*. The vast majority of CC binaries have prograde mutual orbits (i.e., mutual orbital rotations in the same direction as their heliocentric orbits), which is also true for JY<sub>31</sub>, although its orbital inclination is relatively large ( $61^\circ 34 \pm 1^\circ 34$ ). However, the *New Horizons*

search was certainly biased toward equal-sized binaries because those were the only types that could be detected. That, and other selection effects (e.g., optical resolution limits), might suggest that the reported results on KBO binaries generally provide *lower limits* to the true binary fraction.

An independent analysis of the CC population’s binary fraction has been offered based on a systematic analysis of 212 CCs observed by the *Hubble Space Telescope* (Parker et al. 2020). A careful observational debiasing of this sample taking into account the CC luminosity function, binary formation models, and binary colors suggests that the intrinsic binary fraction for objects larger than 30 km and semi-major axes larger than 3000 km is likely lower: 13-16% for  $H_0 < 6.2$  and 1-4% for  $H_0 > 6.2$ . However, this survey is limited to significantly brighter objects than our *New Horizons* sample. Additional analysis by Parker (2021) considers what the binary fraction for tight binaries (between contact and 0.5–1% of the Hill radius) might be based on an evaluation of doublet cratering projected from the currently known wide binary population and results from the simulations of tidal circularization timescales for small KBOs by Porter & Grundy (2012). Parker concludes that while the calculation is sensitive to the proposed separation distribution input, there is a high likelihood for a large population of tight binaries, which is consistent with our identification of JY<sub>31</sub> and OS<sub>393</sub> as binaries. Future occultation observations, or observations by *New Horizons* of other small KBOs, may provide additional support for this conclusion.

## 6. SUMMARY

We have taken advantage of the *New Horizons* spacecraft’s passage through the densest portion of the cold classical (CC) Kuiper belt to image five objects (4 CCs and 1 scattered disk KBO) with spatial resolutions of 136-430 km, which is approximately 6-18 times better than possible from *HST*. By adding hundreds of images taken by the LORRI camera in its high resolution mode (1×1 format), we reached a sensitivity limit of  $V \approx 17$  and detected all five KBOs. Adopting reasonable assumptions, we demonstrated that the CC KBO JY<sub>31</sub> is almost certainly a binary system with two equally bright bodies in a nearly circular orbit with a separation of  $198.6 \pm 2.9$  km and an orbital period of  $1.940 \pm 0.002$  d.

We conclude that the CC KBO OS<sub>393</sub> is also likely a binary with the bodies separated by  $\sim 150$  km. However, the low SNR ( $\approx 5-7$ ) for the OS<sub>393</sub> detections during the first epoch, and the lack of detection during the second epoch (likely explained because OS<sub>393</sub> was near a minimum in its lightcurve, which put the object below LORRI’s detection limit), lowers our confidence level in claiming that OS<sub>393</sub> is a binary system. Future stellar occultation opportunities (Porter et al. 2022) should provide further information on the binary nature of OS<sub>393</sub>.

Both HK<sub>103</sub> (SD) and HZ<sub>102</sub> (CC) were easily detected in the LORRI 1×1 images, but neither appears to be a resolved binary based on our analysis. Our observations rule out equal brightness binaries at separations  $>430$  km for HK<sub>103</sub> and  $>260$  km for HZ<sub>102</sub>. The CC KBO PN<sub>70</sub> was only marginally detected (SNR  $\approx 2.3-3.5$ ) in the LORRI images, precluding definitive statements about its binarity.

In summary, at least one of four, and probably two of four, of the CC KBOs discussed here are binaries. Furthermore, these binaries have the tightest orbits of any resolved KBO binary systems, demonstrating another unique capability of the *New Horizons* program in its exploration of the Kuiper belt. Our results extend to smaller bodies and to smaller semimajor axes the findings from previous studies (Fraser et al. 2017a,b; Noll et al. 2020) that a significant fraction ( $\geq 20\%$ ) of the CC KBO population is comprised of binaries.

This work was supported by NASA's *New Horizons* project through contracts NASW-02008 and NAS5-97271/TaskOrder30. We thank Susan Bennechi, Will Grundy, Alan Stern, and Anne Verbiscer for their detailed comments on earlier drafts of the paper, and we thank Tod Lauer for independently confirming the non-PSF nature of JY<sub>31</sub> and OS<sub>393</sub>. We thank the *New Horizons* Mission Operations team (especially Alice Bowman, Omar Custodio, Helen Hart, and Karl Whittenburg), the *New Horizons* Science Operations team (Debi Rose, Nicole Martin, Ann Harch, and Emma Birath), and the GNC lead (Gabe Rogers) for their expert planning and execution of these complicated observations. We also thank two anonymous reviewers, whose suggested changes improved the paper.

*Software:* Interactive Data Language (IDL), licensed by the Harris Corporation, SciPy ([Virtanen et al. 2020](#)), emcee package ([Foreman-Mackey et al. 2013](#)), HOTPANTS ([Becker 2015](#)), spiceypy package ([Annex et al. 2020](#)).

## REFERENCES

- Annex, A., Pearson, B., Seignovert, B., et al. 2020, *The Journal of Open Source Software*, 5, 2050, doi: [10.21105/joss.02050](https://doi.org/10.21105/joss.02050)
- Becker, A. 2015, ascl:1504.004, <http://ascl.net/1504.004>
- Benecchi, S. D., Borncamp, D., Parker, A. H., et al. 2019, *Icarus*, 334, 22, doi: [10.1016/j.icarus.2019.01.025](https://doi.org/10.1016/j.icarus.2019.01.025)
- Cheng, A. F., Weaver, H. A., Conard, S. J., et al. 2008, *SSRv*, 140, 189, doi: [10.1007/s11214-007-9271-6](https://doi.org/10.1007/s11214-007-9271-6)
- Foreman-Mackey, D., Hogg, D. W., Lang, D., & Goodman, J. 2013, *PASP*, 125, 306, doi: [10.1086/670067](https://doi.org/10.1086/670067)
- Foreman-Mackey, D., Farr, W., Sinha, M., et al. 2019, *The Journal of Open Source Software*, 4, 1864, doi: [10.21105/joss.01864](https://doi.org/10.21105/joss.01864)
- Fraser, W. C., Bannister, M. T., Pike, R. E., et al. 2017a, *Nature Astronomy*, 1, 0088, doi: [10.1038/s41550-017-0088](https://doi.org/10.1038/s41550-017-0088)
- . 2017b, *Nature Astronomy*, 1, 0138, doi: [10.1038/s41550-017-0138](https://doi.org/10.1038/s41550-017-0138)
- Gladman, B., Marsden, B. G., & Vanlaerhoven, C. 2008, *Nomenclature in the Outer Solar System*, ed. M. A. Barucci, H. Boehnhardt, D. P. Cruikshank, A. Morbidelli, & R. Dotson, 43
- Grundy, W. M., Noll, K. S., Virtanen, J., et al. 2008, *Icarus*, 197, 260, doi: [10.1016/j.icarus.2008.04.004](https://doi.org/10.1016/j.icarus.2008.04.004)
- Grundy, W. M., Noll, K. S., Roe, H. G., et al. 2019, *Icarus*, 334, 62, doi: [10.1016/j.icarus.2019.03.035](https://doi.org/10.1016/j.icarus.2019.03.035)
- Grundy, W. M., Bird, M. K., Britt, D. T., et al. 2020, *Science*, 367, aay3705, doi: [10.1126/science.aay3705](https://doi.org/10.1126/science.aay3705)
- Hofgartner, J. D., Buratti, B. J., Benecchi, S. D., et al. 2021, *Icarus*, 356, 113723, doi: [10.1016/j.icarus.2020.113723](https://doi.org/10.1016/j.icarus.2020.113723)
- Jorda, L., Gaskell, R., Capanna, C., et al. 2016, *Icarus*, 277, 257, doi: [10.1016/j.icarus.2016.05.002](https://doi.org/10.1016/j.icarus.2016.05.002)
- Lacerda, P., Fornasier, S., Lellouch, E., et al. 2014, *ApJL*, 793, L2, doi: [10.1088/2041-8205/793/1/L2](https://doi.org/10.1088/2041-8205/793/1/L2)
- McKinnon, W. B., Richardson, D. C., Marohnic, J. C., et al. 2020, *Science*, 367, aay6620, doi: [10.1126/science.aay6620](https://doi.org/10.1126/science.aay6620)
- Nesvorný, D., Li, R., Simon, J. B., et al. 2021, *The Planetary Science Journal*, 2, 27, doi: [10.3847/PSJ/abd858](https://doi.org/10.3847/PSJ/abd858)
- Nesvorný, D., Li, R., Youdin, A. N., Simon, J. B., & Grundy, W. M. 2019, *Nature Astronomy*, 3, 808, doi: [10.1038/s41550-019-0806-z](https://doi.org/10.1038/s41550-019-0806-z)
- Noll, K., Grundy, W. M., Nesvorný, D., & Thirouin, A. 2020, *Trans-Neptunian binaries (2018)*, ed. D. Prialnik, M. A. Barucci, & L. Young, 201–224, doi: [10.1016/B978-0-12-816490-7.00009-6](https://doi.org/10.1016/B978-0-12-816490-7.00009-6)
- Noll, K. S., Grundy, W. M., Chiang, E. I., Margot, J. L., & Kern, S. D. 2008a, *Binaries in the Kuiper Belt*, ed. M. A. Barucci, H. Boehnhardt, D. P. Cruikshank, A. Morbidelli, & R. Dotson, 345
- Noll, K. S., Grundy, W. M., Stephens, D. C., Levison, H. F., & Kern, S. D. 2008b, *Icarus*, 194, 758, doi: [10.1016/j.icarus.2007.10.022](https://doi.org/10.1016/j.icarus.2007.10.022)
- Parker, A., Benecchi, S., Grundy, W., et al. 2020, in *AAS/Division for Planetary Sciences Meeting Abstracts, Vol. 52, AAS/Division for Planetary Sciences Meeting Abstracts*, 307.01
- Parker, A. H. 2021, *Transneptunian Space and the Post-Pluto Paradigm*, ed. S. A. Stern, J. M. Moore, W. M. Grundy, L. A. Young, & R. P. Binzel (Univ. of Arizona, Tucson), 545–568, doi: [10.2458/azu\\_uapress.9780816540945-ch023](https://doi.org/10.2458/azu_uapress.9780816540945-ch023)
- Porter, S., Weaver, H., Verbiscer, A., et al. 2020, in *AAS/Division for Planetary Sciences Meeting Abstracts, Vol. 52, AAS/Division for Planetary Sciences Meeting Abstracts*, 307.03
- Porter, S. B., & Grundy, W. M. 2012, *Icarus*, 220, 947, doi: [10.1016/j.icarus.2012.06.034](https://doi.org/10.1016/j.icarus.2012.06.034)
- Porter, S. B., Spencer, J. R., Benecchi, S., et al. 2016, *ApJL*, 828, L15, doi: [10.3847/2041-8205/828/2/L15](https://doi.org/10.3847/2041-8205/828/2/L15)
- . 2022, accepted by *Planetary Science Journal*
- Rogers, G. D., Flanigan, S. H., Bushman, S., et al. 2016, *New Horizons Guidance & Control & Propulsion Systems Budget Versus Performance for the Pluto Encounter*, ed. D. A. Chart, 959–970
- Spencer, J. R., Buie, M. W., Parker, A. H., et al. 2015, in *European Planetary Science Congress, EPSC2015–417*

- Spencer, J. R., Stern, S. A., Moore, J. M., et al. 2020, *Science*, 367, aay3999, doi: [10.1126/science.aay3999](https://doi.org/10.1126/science.aay3999)
- Stern, S. A., Grundy, W. M., McKinnon, W. B., Weaver, H. A., & Young, L. A. 2018, *ARA&A*, 56, 357, doi: [10.1146/annurev-astro-081817-051935](https://doi.org/10.1146/annurev-astro-081817-051935)
- Stern, S. A., Weaver, H. A., Spencer, J. R., et al. 2019, *Science*, 364, aaw9771, doi: [10.1126/science.aaw9771](https://doi.org/10.1126/science.aaw9771)
- Verbiscer, A. J., Porter, S., Benecchi, S. D., et al. 2019, *AJ*, 158, 123, doi: [10.3847/1538-3881/ab3211](https://doi.org/10.3847/1538-3881/ab3211)
- Verbiscer, A. J., Porter, S. B., Benecchi, S., et al. 2022, submitted to *Planetary Science Journal*
- Vilenius, E., Kiss, C., Müller, T., et al. 2014, *A&A*, 564, A35, doi: [10.1051/0004-6361/201322416](https://doi.org/10.1051/0004-6361/201322416)
- Virtanen, P., Gommers, R., Burovski, E., et al. 2020, doi: [10.5281/zenodo.4100507](https://doi.org/10.5281/zenodo.4100507)
- Weaver, H. A., Cheng, A. F., Morgan, F., et al. 2020, *Proc. Astron. Soc. Pacific*, 132, 035003, doi: [10.1088/1538-3873/ab67ec](https://doi.org/10.1088/1538-3873/ab67ec)
- Weaver, H. A., J., Porter, S. B., Spencer, J. R., et al. 2019, in *AGU Fall Meeting Abstracts*, Vol. 2019, P33I–3531